

## MIT Open Access Articles

*Humoral signatures of protective and pathological SARS-CoV-2 infection in children*

The MIT Faculty has made this article openly available. **Please share** how this access benefits you. Your story matters.

**Citation:** Bartsch, Yannic C. et al. "Humoral signatures of protective and pathological SARS-CoV-2 infection in children." *Nature Medicine* 27, 3 (February 2021): 454–462. © 2021 The Author(s)

**As Published:** <http://dx.doi.org/10.1038/s41591-021-01263-3>

**Publisher:** Springer Science and Business Media LLC

**Persistent URL:** <https://hdl.handle.net/1721.1/131258>

**Version:** Author's final manuscript: final author's manuscript post peer review, without publisher's formatting or copy editing

**Terms of Use:** Article is made available in accordance with the publisher's policy and may be subject to US copyright law. Please refer to the publisher's site for terms of use.



## Humoral signatures of protective and pathological SARS-CoV2 infection in children

Yannic C Bartsch<sup>1#</sup>, Chuangqi Wang<sup>2#</sup>, Tomer Zohar<sup>1,2</sup>, Stephanie Fischinger<sup>1</sup>, Caroline Atyeo<sup>1</sup>, John Burke<sup>1</sup>, Jaewon Kang<sup>1</sup>, Andrea G Edlow<sup>3</sup>, Alessio Fasano<sup>4</sup>, Eric J Nilles<sup>5</sup>, Ann E Woolley<sup>5</sup>, Elizabeth Wood Karlson<sup>5</sup>, Alex R Hopke<sup>6</sup>, Daniel Irimia<sup>6</sup>, Eric S Fischer<sup>7,8</sup>, Edward T. Ryan<sup>6</sup>, Richelle Charles<sup>6</sup>, Boris D. Julg<sup>1</sup>, Douglas A Lauffenburger<sup>2</sup>, Lael M Yonker<sup>4\*</sup> and Galit Alter<sup>1\*</sup>

<sup>1</sup>Ragon Institute of MGH, MIT and Harvard, Cambridge, MA, USA.

<sup>2</sup>Department of Biological Engineering, Massachusetts Institute of Technology, Cambridge, MA, USA.

<sup>3</sup>Massachusetts General Hospital Department of Obstetrics and Gynecology, Division of Maternal-Fetal Medicine, Boston, MA

<sup>4</sup>Massachusetts General Hospital, Mucosal Immunology and Biology Research Center, Boston, MA  
Massachusetts General Hospital, Department of Pediatrics, Boston, MA

<sup>5</sup>Brigham and Women's Hospital, Boston, MA

<sup>6</sup>Massachusetts General Hospital, BioMEMS Resource Center, Boston, MA.

<sup>7</sup>Department of Cancer Biology, Dana Farber Cancer Institute, Boston MA.

<sup>8</sup>Department of Biological Chemistry and Molecular Pharmacology, Harvard Medical School, Boston, MA.

# Co-Author

\* Correspondence:

Galit Alter: galter@mgh.harvard.edu & Lael Yonker: LYONKER@mgh.harvard.edu

## **Abstract**

The SARS-CoV-2 pandemic continues to spread relentlessly, associated with a high frequency of respiratory failure and mortality especially in elderly individuals. Conversely, children experience largely pauci or asymptomatic disease, with rare but alarming reports of a Multisystem Inflammatory Syndrome in Children (MIS-C). Identifying immune mechanisms that result in these disparate clinical phenotypes in children could provide critical insights into the humoral mechanisms underlying asymptomatic, non-pathological disease and point to new strategies to prevent disease. Using Systems Serology, here we observed that children generate a functional IgG response to SARS-CoV-2, comparable to the responses generated in adults with mild and asymptomatic disease. Conversely, IgA and neutrophil responses were significantly expanded in adults with severe disease. Moreover, weeks after the resolution of infection, children who develop MIS-C maintained highly inflammatory monocyte activating SARS-CoV-2 IgG antibodies, which may contribute to a pathomechanistic severe inflammatory syndrome. Collectively, these data provide unique insights into the potential mechanisms of IgG and IgA that may underlie differential disease severity as well as unexpected complications in SARS-CoV-2 infected children.

## Introduction

The SARS-CoV-2 pandemic remains an enormous global challenge due to its persistent spread and unpredictable disease course. While adults can exhibit moderate to severe disease with high mortality, children surprisingly experience largely benign disease characterized by mild cold-like symptoms despite high viral loads<sup>1-3</sup>. Several hypotheses for this disparate phenotype have emerged, including the presence of lower Angiotensin converting enzyme 2 (ACE2) receptor expression in children that may render them less infectable<sup>3</sup>, the potential for pre-existing cross-coronavirus humoral immunity that may attenuate early infection<sup>4,5</sup>, and the potential for a more naïve immune repertoire. A small but significant fraction of SARS-CoV-2-infected or exposed children develop a Kawasaki-disease (KD)-like syndrome, now termed Multisystem Inflammatory Syndrome in Children (MIS-C)<sup>6-8</sup>. Weeks after SARS-CoV-2 exposure or infection, children with MIS-C present with fever, laboratory markers of inflammation, and multi-organ involvement which can include, hypotensive shock, cardiac aneurysms, and ventricular failure<sup>9</sup>.

Emerging data have linked the humoral immune response to SARS-CoV-2 in adults to both protection as well as pathology<sup>10</sup>. To begin to define whether differences in the humoral immune response may account for differences in severity of disease across adults and children and point to pathological changes in MIS-C, here we deeply profiled the functional humoral immune response in 60 adults with acute SARS-CoV-2 infection (26 severe, 34 mild), 25 children with acute but mild SARS-CoV-2 infection, and 17 children who developed MIS-C (11 severe, 6 mild). The data point to a pathological role for SARS-CoV-2-specific IgA responses linked to neutrophil activation in severe adult infection, which do not evolve in children or in mildly infected adults. Conversely, sustained levels of inflammatory macrophage-activating, Fc-receptor binding antibodies were selectively maintained in severe MIS-C disease, across different pathogens. Collectively, these data identify unique functional



antibody responses that leverage neutrophils and/or macrophages in SARS-CoV-2 disease pathology, revealing biomarkers and pathways to guide clinical care and therapeutic development.

## Results

Within days of symptom onset, SARS-CoV-2-specific antibodies are detectable, marking SARS-CoV-2 exposure. However, beyond their absolute quantities, shifts in polyclonal antibody composition mark different responses to infection and disease trajectory<sup>11</sup>. Whether the polyclonal antibody composition differs across adults and children, the latter who largely experience asymptomatic to mild disease, is currently unknown. Thus, we comprehensively profiled the SARS-CoV-2-specific humoral immune response across a group of acutely infected adults and children, including 25 paucisymptomatic children/young adults (ages 0-21 years, median = 15y) compared to 34 adults (ages 22-76 years, median = 34y) with mild disease which did not require hospitalization, and 26 adults (age range: 32-79years, median = 56y) with more severe SARS-CoV-2 infection and all of whom required hospitalization (**Supplemental Table 1**). Acute SARS-CoV-2 infection was diagnosed by related symptoms and positive PCR and/or serology.

### *Low IgA and phagocytic activity track with mild disease in children and adults*

As expected, high titers of SARS-CoV-2 spike (S)-specific IgM, IgG and IgA titers were observed in adults with severe infection (**Figure 1A and B**). Conversely, comparable levels of S-specific IgG and IgM were present in paucisymptomatic children and adults with mild acute infection. In contrast to more attenuated but similar SARS-CoV-2 receptor-binding domain (RBD), spike (S) and nucleocapsid (N)-specific isotype, subclass, and Fc-receptor binding levels in children and adults with mild disease, severely ill patients exhibited robustly expanded humoral immune responses (**Figure 1B and Supplemental Figure 1-3**). Next, we tested the ability of plasma antibodies to induce Fc-mediated effector function. Antigen:antibody immune-complexes (ICs) were generated by incubating plasma with antigen-coated fluorescent beads, and ICs were then cultured with complement, THP-1 monocytes or HL60 differentiated neutrophils to analyze complement deposition or phagocytic activity. Similar levels of complement, neutrophil, and monocyte activating antibodies were observed in children and mildly infected adults, in contrast to adults with severe infection (**Figure 1C and**

**Supplemental Figure 4**). Interestingly, pediatric patients exhibited a tendency to develop antibodies earlier after symptom onset compared to adults, potentially contributing to reduced pathology and differences in kinetics of overall symptomatology across the ages (**Supplemental Figure 5**), however responses in children were similar to those observed in adults that experienced mild disease (**Figure 1A and B**). These data suggest that children may not necessarily make a stronger or more effective functional humoral immune response compared to adults.

To next determine whether any multivariate differences exist among the adult and pediatric profiles of seropositive individuals, an unsupervised Uniform Manifold Approximation and Projection (UMAP) was initially used to collapse the multivariate data into 2 dimensions, with proximity representing similarities in the overall dataset. Separation was observed visually across children and severely ill individuals in the UMAP, pointing to substantial global humoral profile differences across the groups (**Figure 2A**). Similarly, discrete antibody profiles were observed across severely and mildly ill adults (**Figure 2B**). In contrast, adults with mild disease and children overlapped extensively, highlighting the multivariate similarity in the overall SARS-CoV-2 antibody profiles between the groups (**Figure 2C**). The integration of all 3 groups in a single UMAP further highlighted the similarity in mild disease antibody profiles among adults and children, that were largely distinct, albeit along a continuum, from those in severely ill adults, suggesting that severity of disease, rather than age, may influence antibody profiles predominantly (**Supplemental Figure 6**).

To further define the individual features that distinguished children or adults with mild infection to adults with severe disease, we used Least Absolute Shrinkage and Selection Operator (LASSO) feature selection to initially reduce the total 48 antibody variables to a minimal set that represented the overall variation in the antibody profiles, followed by classification using Partial Least-Squares Discriminant Analysis (PLS-DA). Nearly perfect separation was observed between children and severely ill adults (**Figure 2D**). The model used only 5 of the total 48 measured features to resolve the 2 groups, including RBD-specific-neutrophil phagocytosis, N-specific IgA2 levels and monocyte phagocytosis enriched in severely ill adults, and RBD-specific monocyte phagocytosis in

children. These data point to significantly expanded IgA and phagocytic functional responses in severely ill individuals, suggesting IgA-driven immune complex phagocyte activation as a marker of disease severity. Likewise, near complete separation was observed between adults with mild and severe disease (**Figure 2E**), marked again by high levels of monocyte phagocytic functions, IgA2 responses, and S-specific binding to FcγR3b expressed on neutrophils, neutrophils phagocytosis, as well as complement activation and IgM titer. In contrast, antibody profiles between children and adults with mild disease could not be resolved (**Figure 2F**).

A correlation network was constructed between LASSO-selected features and the overall immune response to deeply probe the distinct relationships that diverged between severe and mild disease (**Figure 2G and Supplemental Figure 7**). N-specific IgA, N-, S-, and RBD-specific Fcα-receptor (FcαR) binding (found constitutively on neutrophils<sup>12</sup>), neutrophil phagocytosis and complement activation were all induced in a synchronized manner, pointing to a central axis of IgA:neutrophil activation in severe disease. Moreover, while depletion of IgG, our dominant serum antibody, resulted in attenuated neutrophil phagocytosis, depletion of IgA also reduced ADNP significantly among severely ill individuals (**Figure 3A-C**). Moreover, while depletion of IgG was sufficient to eliminate ADNP in mild adults and children (**Figure 3A and C**), combined depletion of IgG and IgA resulted in complete loss of ADNP in severe adults (**Figure 3C**), pointed to an added role of IgA in neutrophil activation in severe disease.

Given our emerging appreciation for excessive neutrophil activity in COVID-19 pathology<sup>13,14</sup>, we further probed the functional role of IgA in neutrophil IC-responsiveness. Despite the pronounced effect of IgG in attenuating phagocytosis, the depletion of both IgG and IgA resulted in a loss of neutrophil degranulation of myeloperoxidase (MPO), lactoferrin and matrix metalloproteinase-9 (MMP-9), as well as attenuated cytokine secretion (**Figure 3D and Supplemental Figure 8**).

Specifically, compared to IgG depletion, elimination of IgA further decreased tertiary MMP-9 granule, interleukin-1β (IL-1β), IL-6, and IL-8 release from neutrophils (**Figure 3D**), resulting in a unique IgA-driven multivariate functional cascade marked by enhanced inflammatory neutrophil activity in the

presence of SARS-CoV-2-specific IgA (**Figure 3E**), as has been noted previously<sup>15,16</sup>. Furthermore, longitudinal profiling of an orthogonal cohort of hospitalized individuals pointed to the selective evolution of enhanced IgA2 levels in severely ill individuals, particularly 1 week after symptom onset, linked to disproportionately higher levels of Fc $\alpha$ R binding and ADNP activity (**Figure 3F**), potentially implicating IgA2 emergence as a unique mechanistic marker of severe SARS-CoV-2 disease. Thus, collectively these data point to a unique and robust involvement of IgA-driven functions in severe disease, that do not evolve in children or adults with mild disease.

#### *Persistence of inflamed SARS-CoV-2 antibodies track with MIS-C*

Despite the largely mild nature of pediatric SARS-CoV-2 infection, a subset of children develop a severe inflammatory-mediated illness after infection, MIS-C, including potential antibody-driven immunopathology similar to KD<sup>6,8</sup>. While early data has pointed to differences in IgM levels in children with MIS-C compared to acutely infected adults and children<sup>17</sup>, this loss of IgM could simply be attributable to the resolution of infection in MIS-C that occurs weeks after infection. Thus, to begin to delineate whether particular polyclonal antibody signatures could provide mechanistic insights into MIS-C disease and pathology, SARS-CoV-2 specific humoral immunity was profiled across children with mild or severe MIS-C compared to a group of non-hospitalized convalescent adults who had mild disease symptoms (not hospitalized and no oxygen therapy required), the latter matched for time (days from symptom onset: 11- 38, median: 27 days) from suspected infection (**Figure 4 and Supplemental Table 1**). A total of 17 children/young-adults (0 -21.9 years, median 3.5y, 83 % male) were diagnosed with MIS-C per CDC criteria (reference: <https://www.cdc.gov/mis-c/hcp/>): patients had fever, laboratory evidence of inflammation, multisystem involvement that required hospitalization, plus evidence of SARS-CoV-2 infection (positive SARS-CoV-2 RT-PCR or antigen test, or positive SARS-CoV-2 antibodies) or SARS-CoV-2 exposure, with no alternative diagnosis. Of note, one of our patients was 21.9 years old but otherwise met CDC MIS-C criteria. Patients with MIS-C were stratified by MIS-C severity with severe patients defined as experiencing cardiac complications

(see Methods and **Supplemental Table 2**). The severe MIS-C cohort exhibited comparable IgM and IgG1 titers to those observed in convalescents. Conversely, despite a positive RT-PCR result in 50% of the children, SARS-CoV-2 antibodies were not detectable in the majority of mild MIS-C cases (only one child in this group had detectable levels of S and RBD-specific IgG3 and IgA1; **Figure 4A and Supplemental Figure 1-3**). Focusing on convalescent adults and severe MIS-C children, that both harbored robust SARS-CoV-2 humoral immune responses weeks after infection, a broad isotype, subclass, and functional antibody profile was observed across the groups (**Figure 4B and Supplemental Figure 4**), although the specific expanded humoral features differed across the groups (**Figure 4B**). For example, while similar levels of complement deposition and neutrophil phagocytosis were observed in the convalescent adults and severe MIS-C cases (**Figure 4B and C**), MIS-C cases exhibited enhanced monocyte activating capacity (**Figure 4C**). This suggests convalescent-like profiles in the severe MIS-C cases, but the presence of a select set of altered antibody features that uniquely emerge in this pathological setting.

To gain deeper insights into the specific immune alterations that define MIS-C, we next performed multivariate analysis. Clear separation was observed in the multivariate SARS-CoV-2 response in mild and severe MIS-C (**Figure 5A**) both by UMAP and LASSO/PLSDA, simply driven by the presence of SARS-CoV-2-specific IgG and IgM responses in the severe cases. Interestingly, severe MIS-C cases were distinguishable from both convalescent adults (**Figure 5B**) and mild children (**Figure 5C**) largely linked to higher SARS-CoV-2-specific antibody titers with more phagocytic and functional activity distinct from immune responses in severe acute disease in adults (**Supplemental Figure 9**). Network analysis highlighted the over-representation of functional humoral immune responses in the MIS-C children, pointing to a potential IC based activity in disease pathology (**Figure 5D**). Additionally, comparison of MIS-C children to adults with severe acute disease revealed distinct antibody profiles across the 2 groups, with expanded IgG driven function in MIS-C and IgA/neutrophil expanded immune responses in the severe adults, pointing to a persistent IgG related disease in MIS-C (**Supplemental Figure 10**)<sup>17</sup> and IgA related disease in acute SARS-CoV-2 infection.

However, why the children with MIS-C maintained a response able to continue to recruit a SARS-CoV-2-specific phagocytic and complement activating response remains unclear, but collectively points to more inflamed antibody profiles among severe MIS-C cases. Strikingly, this inflamed antibody profile was not only observed in the SARS-CoV-2 specific humoral immune response: as shown in **Figure 5E (and Supplemental Figure 11)**, an expansion of highly functional antibodies were observed across multiple diverse other pathogens that have been implicated, but not proven to drive, KD (EBV, measles, endogenous retrovirus (ERV), *B. pertussis* and *S. aureus*), auto-antigens linked to MIS-C (personal communication) common respiratory pathogens (influenza and RSV) - as well as to common-coronaviruses (CoVs, strains: OC43, 229E, HKU1 and NL63)<sup>1819</sup>. While no difference was observed in overall IgG levels (**Supplemental Figure 12**), these findings point to a significantly expanded Fc-receptor binding humoral antibody repertoire among severe MIS-C cases, but not in severe acute adult cases (**Figure 5E and Supplemental Figure 11**), in the absence of hypergammaglobulinemia, pointing to a significant non-specific amplification of functional pathogen-specific IgG driven immunity, able to drive broad inflammation. Together these data argue for a generalized dysregulated pro-inflammatory IgG-response to SARS-CoV-2 and beyond in severe MIS-C.

## Discussion

The unpredictable nature of SARS-CoV-2 disease severity is alarming, with rare but severe acute-disease emerging in adults and a KD-like MIS-C syndrome in children<sup>8</sup>. In the absence of therapeutics able to reverse these clinical manifestations, understanding the immunological mechanisms that underlie these unusual complications of SARS-CoV-2 infection may provide critical insights for the design and delivery of therapeutics for these unique populations. Here we note divergent, but unique humoral immune profiles among mild symptomatic children/young adults and children with severe MIS-C that implicate distinct humoral immune functions in disease pathology. The induction of SARS-CoV-2-specific IgA responses, linked to neutrophil activation, was enriched in

severely ill adults, but was less pronounced in the humoral immune response in children and mildly affected adults. Conversely, children that developed MIS-C exhibited persistent, enhanced Fc-receptor binding antibodies, poised to recruit monocytes in a selective manner.

Beyond the pivotal role of IgG mediated functions, IgA is the most highly produced antibody isotype in the body (66 mg/kg/day), and while highly enriched at mucosal surfaces<sup>20</sup>, serum IgA has emerged as a highly potent activator of innate immune effector function<sup>21</sup>. In the blood, immune complexes including IgA interact with Fc $\alpha$ R, constitutively expressed on neutrophils, but also upregulated on several mucosal immune cell subsets. While neutrophils also express Fc-receptors for IgG, both IgA and IgG result in different neutrophil functions, where IgG drives phagocytosis and cytokine secretion and IgA can augment these functions and additionally drive robust degranulation, cytokine secretion, and NETosis<sup>22</sup>. Along these lines, depletion of both IgG and IgA resulted in attenuated neutrophil activation, however, the depletion of IgA resulted in more robust attenuation of tertiary degranulation and cytokine release. Thus, in addition to IgG, elevated IgA levels, observed in adults with more severe disease<sup>23</sup> may be linked to enhanced disease severity via the recruitment of Fc $\alpha$ R driven inflammatory cascades downstream of phagocytosis (**Figure 1 and Supplemental Figure 1-3**). Given the presence of IgG, but not IgA responses in both children and adults with mild disease, the data potentially argue that IgG alone may be sufficient to control and contain the infection in mild infection.

While IgA could simply represent a biomarker of enhanced viremia in the lung, IgA is thought to play a critical role in mucosal immunity. However, the potent inflammatory activity of IgA may also contribute to enhanced inflammation that may contribute to symptomatic disease in adults. Interestingly, sero-surveillance studies in otherwise healthy children have shown that IgA levels increase with age peaking in the late teenage years in the blood<sup>24</sup>. Conversely, children have been noted to have more severe disease following other respiratory infections including influenza, pertussis, respiratory syncytial virus, and group B streptococci<sup>25</sup>, hypothesized to be related to the lower capacity to generate IgA. While it is critical to note that children with MIS-C generated SARS-



CoV-2 IgA responses, these responses tended to be lower than those observed in adults (Supplemental Figure 1-4). Thus collectively, these data may point to a potentially unexpected pathological role of IgA in adult SARS-CoV-2 infection, that may contribute to enhanced disease in the elderly, via the over-activation of neutrophil degranulation and inflammation.

Children diagnosed with MIS-C, conversely, exhibited a persistence of functional SARS-CoV-2-specific monocyte-activating antibodies and expanded pan-pathogen FcγR binding antibodies, in the absence of hypergammaglobulinemia (Supplemental Figure 12). Given that monocyte activation and immune-complexes have both been associated with KD disease severity<sup>26,27</sup>, these data point to potential mechanistic disease associated parallels between KD and MIS-C. Moreover, similar to enhanced FcγR2a binding observed here in MIS-C, FcγR2a, a receptor essential for monocyte phagocytosis<sup>28</sup>, has been described as a susceptibility locus for KD<sup>29</sup>. Furthermore, effective IVIG treatment of KD has been linked to direct inhibition of FcγR2a mediated immune-complex activation<sup>30,31</sup>, further supporting the importance of FcγR binding antibodies in this pediatric disease.

As reported for other MIS-C cases<sup>32</sup>, none of our mild MIS-C cases had SARS-CoV-2 titers but experienced more symptoms including a cough (3 out of 6 vs. 2 of 11 in severe MIS-C). Conversely, as expected, most of our severe MIS-C cases were seropositive for SARS-CoV-2, 2 children lacked antibodies, thus we cannot exclude that these were KD cases. Nevertheless, MIS-C disease severity was clearly associated with exposure and antibodies against SARS-CoV-2 for the majority of the cases in our cohort. However, most notable was the maintenance of SARS-CoV-2 immunity among the severe MIS-C cases over time (Supplemental Figure 10)<sup>17</sup>, despite emerging reports of rapid humoral waning in adults<sup>33</sup>. Similarly, humoral immune responses were nearly undetectable in most children with mild MIS-C disease, but persisted at high levels in severe cases, comparable to levels in previously mildly symptomatic convalescent adults. Conversely, whether persisting functional-antibodies is the result of sustained viral replication in these children, or related to an aberrant persisting germinal center reaction, persistent specific immune complexes, or an overall activation of the humoral immune response remains unclear. Yet, a recent report of non-specific plasmablast

expansion in MIS-C, together with elevated levels of IL-6, IL-10 and TNF $\alpha$ , all of which can drive B cell proliferation, support the observed non-specific B cell activation in MIS-C reported here<sup>34-36</sup>.

However, here we did not observe evidence of hypergammaglobulinemia in children with MIS-C or drastic shifts in antibody glycosylation (**Supplemental Figure 12**), both associated with autoimmune disease and aberrant humoral immunity, but did exhibit elevated responses to several respiratory, common coronaviruses, other pathogens previously associated with KD, or auto-antigens previously linked to aberrant MIS-C<sup>19</sup>, pointing to a potential overactivated, but not generally enhanced, humoral immune response. Interestingly, IgG1, but not IgM, titers were expanded in children with severe MIS-C, potentially indicating a predominant reactivation of previously primed B cells, rather than the elicitation of novel B cell responses. Moreover, expanding IgG1 and Fc $\gamma$ R titers were highly correlated indicating a generalized more pro-inflammatory potential within the humoral immune response, similar to the response typically observed following a secondary recall response. Given our emerging appreciation for the presence of virus in distal tissues, including the heart and kidney, it is possible that these persisting overactive antibodies may drive tissue-localized macrophage or monocyte activation within these sites, contributing to disease activity.

Taken together, IgA and monocyte-activating antibodies appear to play an unexpected pathological role in COVID-19 and MIS-C, respectively. Given the low probability that children are exposed to less virus that would generally cause less disease in this population, the data argue that severity of disease may be linked to the reduced IgA responses in youth. Conversely, monocyte-activating IgG, rather than IgA, in MIS-C, may contribute to organ-attack via the recognition of SARS-CoV-2 or other pathogen or auto-antigens that all exhibit enhanced and persistent Fc-receptor binding capacity. Thus overall, comparisons of humoral immunity in children provide clues related to the potential pathological functions of antibodies following SARS-CoV-2 infection.

### **Author contribution**

YCB, LMY and GA analyzed and interpreted the data. YCB, TZ, SF CA, JB and JK performed experiments. CW and DAL performed the computational analysis. AGE, AF, EJN, LRB, EWB ER, RC, and LMY collected the samples and supervised and managed the clinical data. AGS and ESF produced SARS-CoV-2 and human coronavirus antigens. LMY and GA supervised the project. YCB and GA drafted the manuscript. All authors critically reviewed the manuscript.

### **Acknowledgement**

LMY received funding from the National Heart Lung and Blood Institute (5K08HL143183), and the Cystic Fibrosis Foundation (YONKER18Q0). DAL was partially supported by the National Institute for Allergy and Infectious Disease (U19 AI135995). NIH R01 AI146779 and a Massachusetts Consortium on Pathogenesis Readiness(MassCPR) was awarded to AGS. We thank Nancy Zimmerman, Mark and Lisa Schwartz, an anonymous donor (financial support), Terry and Susan Ragon, and the SAMANA Kay MGH Research Scholars award for their support. We would also like to thank Yongfei Cai and Bing Chen for S protein production efforts and Jared Feldman, Blake Marie Hauser, Tim Caradonna and Aaron Schmidt for generating receptor binding domain antigens. We acknowledge support from the Ragon Institute of MGH, MIT, the Massachusetts Consortium on Pathogen Readiness (MassCPR), the NIH (3R37AI080289-11S1), “Immune Response to Pathogens” (2007P0002451), Centers for Disease Control and Prevention U01CK0009490, NIH SeroNet U01CA260476, and the Gates foundation Global Health Vaccine Accelerator Platform funding. We would also like to thank Dr. Xu Yu, Alicja Piechocka-Trocha, and Kristina Lefteri for their support on the collection and processing of adult MassCPR cohorts.

### **Conflict of interest**

Galit Alter is a founder of Seromyx Systems. All other authors have declared that no conflict of interest exists.

### **Data availability statement**

All relevant data is included in this manuscript. Additional protocols or raw data will be made available upon request.

### **Code availability statement**

There was no specific custom code used in this manuscript. All code is publicly available, and the source indicated in the text and/or methods section. Scripts will be made available upon request.

## Material and Methods

### Cohort

Plasma samples were obtained from pediatric and adult patients at Massachusetts General Hospital under the Institutional Review Board (IRB)-approved MGH Pediatric COVID-19 Biorepository (#2020P000955). Additionally, plasma samples from adult patients were collected under the IRB-approved 'MGH COVID-19 Biorepository' (#2020P000804) and 'Biorepository for Samples from those at increased risk for or infected with SARS-CoV-2' (#2020P000849). Informed consent, and assent when appropriate, were signed verbally in accordance with IRB guidelines, by the patients or parent/guardian, prior study enrollment. A detailed description of the pediatric cohort characteristics was previously published<sup>3,37</sup>. Patients were diagnosed with COVID-19 related symptoms and positive PCR and/or serology for SARS-CoV-2. MIS-C was diagnosed according to CDC criteria. Severe MIS-C was defined by presence of hypotension or cardiac abnormalities that required intervention including steroids, IVIG and/or anakinra (**Supplemental Table 2**). All analyzed samples were taken before treatment with IVIG.

### Antigens and biotinylation

The receptor binding domains (RBD) of SARS2-CoV-2 and coronavirus strains NL63, HKU1, OC43 and 229 were generously provided by Aaron Schmidt. SARS2-CoV2-S was provided by LakeLake Pharma Inc. SARS2-CoV2-NC (Aalto Bio Reagents Ltd), Flu HAs and EBV p18 (both ImmuneTech Corp), RSV postF (was generously provided from Barney Graham), Measles (Bio-Rad Laboratories), Endogenous retrovirus-W antigen and TSPO (both from Abnova), Pertussis toxin (List Biological Laboratories) CD105 (Novus Biological) and RBPJK (OriGene) were purchased from the different vendors. If indicated, antigens were biotinylated using Sulfo-NHS LCLC biotin (Thermo Fisher) and excessive biotin removed with ZebaSpin desalting columns (7KDa cut-off, Thermo Fisher).

### **IgG subclass, isotype and FcγR binding**

Antigen specific antibody subclass and isotypes, and FcγR binding was further analyzed by Luminex multiplexing. The antigens were coupled to magnetic Luminex beads (Luminex Corp, TX, USA) by carbodiimide-NHS ester-coupling with an individual region per antigen. Coupled beads were incubated with different plasma dilutions (between 1:100 and 1:1,000 depending on the secondary reagent) for 2 hours at room temperature in 384 well plates (Greiner Bio-One, Germany). Unbound antibodies were washed away and subclasses, isotypes were detected with a respective PE-conjugated antibody (all polyclonal, SouthernBiotech, AL, USA). For the FcγR binding a respective PE-Streptavidin (Agilent Technologies, CA, USA) coupled recombinant and biotinylated human FcγR protein was used as a secondary probe. After 1 h incubation, excessive secondary reagent was washed away and the relative antibody concentration per antigen determined by flow cytometer on an IQue analyzer (IntelliCyt, NM, USA). Samples were defined seropositive when they had detectable titer (by Luminex) for IgG1, IgM, and/or IgA1 and a negative cut-off was defined as the average value of SARS-CoV-2 negative samples plus five times the standard deviation. Luminex results for IgG1 were validated by RBD-IgG ELISA as previously described (**Supplemental Figure 13**)<sup>38</sup>.

### **ADCD**

Antibody-Dependent-Complement-Deposition was assessed as described before<sup>39</sup>. In brief, biotinylated antigen was coupled to fluorescence Neutravidin beads (Thermo Fisher). Plasma antibodies were diluted 1:10 in 0.1% BSA and incubated with the coupled antigen beads for 2h at 37°C. Beads were washed and incubated with complement factors from guinea pig for 20 minutes at 37°C. The complement reaction was then stopped by washing with 15mM EDTA in PBS. C3 deposition on the beads was detected with an FITC conjugated anti-guinea pig C3 antibody and relative C3 deposition was analyzed by flow cytometry.

### **ADNP**

For antibody-Dependent Neutrophil Phagocytosis HL-60 cells were differentiated into neutrophils in media containing 1.2 % DMSO for seven days. On the day of the assay, biotinylated antigens were incubated with Neutravidin beads and immune complexes formed by incubation with 1:100 diluted plasma for 2h at 37°C in 96 well plates (Greiner Bio-One). Differentiated HL-60 cells were added afterwards and incubated for 20h at 37°C. Neutrophil phagocytosis was analyzed by flow cytometry and phagocytosis score calculated as the product of frequency bead positive CD11b neutrophils and bead fluorescent intensity (**Supplemental Figure 14**).

#### **ADCP**

THP-1 monocyte phagocytosis was performed as described <sup>40</sup>. Briefly, biotinylated antigens were conjugated to Neutravidin beads and incubated with 1:100 diluted plasma samples. THP-1 monocytes (0.25M cells/well) were added to the immune complexes and incubated for 16h at 37°C, fixed with 4% para-formaldehyde and analyzed by flow cytometry (**Supplemental Figure 14**).

#### **Plasma IgA and IgG depletion**

IgA and or IgG was depleted from human plasma samples using CaptureSelect™ IgA Affinity Matrix and IgG was depleted with Protein A/G Agarose (Thermo Fisher). The capture matrices were washed three times with PBS and incubated over night with 1:5 diluted plasma samples in a low protein binding MultiScreen® filter plate (Millipore). Depleted plasma was recovered by centrifugation of the filter plate and depletion confirmed by ELISA. Non-depleted plasma was treated similarly but without affinity matrix.

#### **Primary neutrophil ADNP**

Neutrophil phagocytic activity of IgA depleted plasma samples was tested on primary human neutrophils <sup>41</sup>. Biotinylated antigens were coupled to fluorescent neutravidin beads (Thermo Fisher) and incubated 1:100 diluted plasma. Primary neutrophils were incubated with immune complexes

for 1h at 37°C. Next, cells were stained for surface CD66b (Biolegend, CA, USA; clone: G10F5) expression, fixed with 4% para-formaldehyde and analyzed by flow cytometry (**Supplemental Figure 14**).

### **Secondary Neutrophil assays**

Blood neutrophils of healthy donors were isolated using EasySep™ Direct Human Neutrophil Isolation Kit (Stemcell Technologies). Neutrophils were stimulated with bead based immune-complexes and supernatants harvested after 4 hours. Supernatants were diluted 1:5 and release of MPO (Thermo Fisher), MMP9 and Lactoferrin (Abcam) were measured using the Human Elisa Kits according to manufacturer's instructions. Cytokines were detected in undiluted supernatant using custom-made multiplex cytokine kit (Thermo Fisher).

### **Plasma isotype ELISA**

Plasma IgG, IgM and IgA concentrations were analyzed by ELISA. Respective goat anti-human capture antibody against IgG, IgM or IgA (5 µg/ml) (all Bethyl Laboratories) were coated to an MaxiSorp 384 well ELISA plates (Thermo Fisher). Unspecific binding sites were blocked with 5% BSA. Plasma samples were diluted 1:500,00 for IgG and 1:50,000 for IgM and IgA. After sample incubation IgG, IgM or IgA was probed with 1:10,000 of HRP conjugated goat anti-human IgG, IgM or IgA antibody (all Bethyl Laboratories). The ELISA was developed with 3,3',5,5'-Tetramethylbenzidine (TMB, Thermo Fisher) and reaction stopped with sulfuric acid. Concentrations were calculated from a two-fold serial dilution curve pooled normal IgG (Bethyl Laboratories) or IgM (Sigma-Aldrich) starting at 125 ng/ml.

### **IgG-Fc glycosylation**

Plasma samples were diluted 1:10 with PBS and incubated overnight at 4°C with magnetic Protein G beads (Millipore). Fab fragments were enzymatically separated from the ProteinG bound Fc parts using IdeZ (NEB). IgG-Fc glycans were released from the protein and APTS labeled with GlycanAssure APTS Kit (Thermo Fisher) and analyzed on 3500xL Genetic Analyzer (Thermo Fisher) capillary



electrophoresis instrument. Glycans were assigned based on retention times of known standard glycans as described before<sup>42</sup>.

### **Computational analysis**

For each paired group, we collected all the measurements from Luminex, functional profiling, and neutralization antibody assays; we eliminated features with missing values across samples. As a quality filter we required features to have values across samples greater than 65% compared to PBS control. The filtered data from Luminex were log transformed by log10 function and all the selected features were scaled and centered.

To visualize relationships between measurements and labels qualitatively, we employed UMAP<sup>43</sup> based methods to compress this high-dimensional serological data into a two-dimensional space. First principle components (PCs) that explain more than 90% of the variance were extracted by principal component analysis (PCA)<sup>44</sup> using the 'prcomp' function in R package 'stats'. Next, the selected PCs were mapped into a two-dimensional space through the UMAP technique implemented using the R package 'umap' with fine-tuning parameters (neighbor = 10, min.dist = 0.1).

Classification models were trained to distinguish different paired groups with a minimal set of features. First, we applied the least absolute shrinkage and selection operator (LASSO) feature selection algorithm, to extract significant features<sup>45</sup>. We ran LASSO 10 times on the whole dataset and identified the features chosen in more than 80% of the repetitions, which were implemented in the function 'select\_lasso' in systemserology R package. A Partial Least-Squares Discriminant Analysis (PLS-DA) classifier was then trained using the extracted features. Model performance was evaluated by five-fold cross-validation, and negative control models were constructed from permuted data with multiple iterations. The permuted control models were generated 20 times by shuffling labels randomly for each repetition. Predicted and true outcomes were compared to determine cross-validation accuracy. The exact P values were calculated as the tail probability of the

true value within the control distributions. For PLS-DA we used the 'opls' function in ropls R package for classification and functions in systemsseRology R package for the purpose of visualization.

We used correlation networks to visualize the additional humoral immune features significantly associated with the selected minimal features, offering enhanced insights of biological mechanisms.

Antibody features that were significantly ( $p$  value  $< 0.05$ ) correlated with a Benjamini-Hochberg correction to the final selected PLS-DA features were defined as co-correlates. Significant spearman correlations about a threshold of  $|r| > 0.7$  were visualized within the networks.

For implementation, spearman correlation coefficients were calculated using 'rcorr' function in 'Hmisc' package and the  $p$  values were corrected by 'Benjamini-Hochberg' correction in 'stats' package. Finally, The correlation networks were properly lay-outed and visualized using 'ggraph' and 'igraph' package with later manual adjustment using Adobe Illustrator.

### **Statistical analysis**

If not stated otherwise, we assumed non-normal distributions and violin plots were generated and statistical differences between two groups were calculated using a two sided Mann Whitney test. To compare multiple groups, a Kruskal-Wallis test was used with a Dunnett test correcting for multiple comparisons in Graph Pad Prism V.8 (significance levels: \*: $p < 0.05$ , \*\*: $p < 0.01$ , \*\*\*: $p < 0.001$ , \*\*\*\*: $p \leq 0.0001$ ). Flower plots were visualized with the ggplot package (v.0.7) and correlation chord diagrams were plotted using circlize package (v.0.4.1) in R (v.4.0.1) and R Studio (v.1.3) and the average of the Z-scored data per variable and group is shown.

## References

- 1 CDC-Covid-Response-Team. Coronavirus Disease 2019 in Children - United States, February 12-April 2, 2020. *MMWR Morb Mortal Wkly Rep* **69**, 422-426, doi:10.15585/mmwr.mm6914e4 (2020).
- 2 Bi, Q. *et al.* Epidemiology and transmission of COVID-19 in 391 cases and 1286 of their close contacts in Shenzhen, China: a retrospective cohort study. *Lancet Infect Dis*, doi:10.1016/S1473-3099(20)30287-5 (2020).
- 3 Yonker, L. M. *et al.* Pediatric SARS-CoV-2: Clinical Presentation, Infectivity, and Immune Responses. *J Pediatr*, doi:10.1016/j.jpeds.2020.08.037 (2020).
- 4 Braun, J. *et al.* SARS-CoV-2-reactive T cells in healthy donors and patients with COVID-19. *Nature*, doi:10.1038/s41586-020-2598-9 (2020).
- 5 Ladner, J. T. *et al.* Epitope-resolved profiling of the SARS-CoV-2 antibody response identifies cross-reactivity with an endemic human CoV. *bioRxiv*, doi:10.1101/2020.07.27.222943 (2020).
- 6 Verdoni, L. *et al.* An outbreak of severe Kawasaki-like disease at the Italian epicentre of the SARS-CoV-2 epidemic: an observational cohort study. *Lancet* **395**, 1771-1778, doi:10.1016/S0140-6736(20)31103-X (2020).
- 7 Riphagen, S., Gomez, X., Gonzalez-Martinez, C., Wilkinson, N. & Theocharis, P. Hyperinflammatory shock in children during COVID-19 pandemic. *Lancet* **395**, 1607-1608, doi:10.1016/S0140-6736(20)31094-1 (2020).
- 8 Feldstein, L. R. *et al.* Multisystem Inflammatory Syndrome in U.S. Children and Adolescents. *N Engl J Med* **383**, 334-346, doi:10.1056/NEJMoa2021680 (2020).
- 9 Belhadj, Z. *et al.* Acute heart failure in multisystem inflammatory syndrome in children (MIS-C) in the context of global SARS-CoV-2 pandemic. *Circulation*, doi:10.1161/CIRCULATIONAHA.120.048360 (2020).
- 10 Zohar, T. & Alter, G. Dissecting antibody-mediated protection against SARS-CoV-2. *Nat Rev Immunol* **20**, 392-394, doi:10.1038/s41577-020-0359-5 (2020).
- 11 Atyeo, C. *et al.* Distinct Early Serological Signatures Track with SARS-CoV-2 Survival. *Immunity*, doi:10.1016/j.immuni.2020.07.020 (2020).
- 12 Hamre, R., Farstad, I. N., Brandtzaeg, P. & Morton, H. C. Expression and modulation of the human immunoglobulin A Fc receptor (CD89) and the FcR gamma chain on myeloid cells in blood and tissue. *Scand J Immunol* **57**, 506-516, doi:10.1046/j.1365-3083.2003.01220.x (2003).
- 13 Veras, F. P. *et al.* SARS-CoV-2-triggered neutrophil extracellular traps mediate COVID-19 pathology. *J Exp Med* **217**, doi:10.1084/jem.20201129 (2020).
- 14 Laforge, M. *et al.* Tissue damage from neutrophil-induced oxidative stress in COVID-19. *Nat Rev Immunol* **20**, 515-516, doi:10.1038/s41577-020-0407-1 (2020).
- 15 Witko-Sarsat, V., Rieu, P., Descamps-Latscha, B., Lesavre, P. & Halbwachs-Mecarelli, L. Neutrophils: molecules, functions and pathophysiological aspects. *Lab Invest* **80**, 617-653, doi:10.1038/labinvest.3780067 (2000).
- 16 Zuo, Y. *et al.* Neutrophil extracellular traps in COVID-19. *JCI Insight* **5**, doi:10.1172/jci.insight.138999 (2020).
- 17 Weisberg, S. P. *et al.* Distinct antibody responses to SARS-CoV-2 in children and adults across the COVID-19 clinical spectrum. *Nat Immunol*, doi:10.1038/s41590-020-00826-9 (2020).
- 18 Menikou, S., Langford, P. R. & Levin, M. Kawasaki Disease: The Role of Immune Complexes Revisited. *Front Immunol* **10**, 1156, doi:10.3389/fimmu.2019.01156 (2019).
- 19 Consiglio, C. R. *et al.* The Immunology of Multisystem Inflammatory Syndrome in Children with COVID-19. *Cell*, doi:10.1016/j.cell.2020.09.016 (2020).
- 20 Fagarasan, S. & Honjo, T. Intestinal IgA synthesis: regulation of front-line body defences. *Nature reviews. Immunology* **3**, 63-72, doi:10.1038/nri982 (2003).
- 21 Woof, J. M. & Kerr, M. A. IgA function--variations on a theme. *Immunology* **113**, 175-177, doi:10.1111/j.1365-2567.2004.01958.x (2004).

- 22 Alejd, E. *et al.* IgA enhances NETosis and release of neutrophil extracellular traps by polymorphonuclear cells via Fc $\alpha$  receptor I. *J Immunol* **192**, 2374-2383, doi:10.4049/jimmunol.1300261 (2014).
- 23 Yu, H. Q. *et al.* Distinct features of SARS-CoV-2-specific IgA response in COVID-19 patients. *Eur Respir J*, doi:10.1183/13993003.01526-2020 (2020).
- 24 Weemaes, C. *et al.* Development of immunoglobulin A in infancy and childhood. *Scand J Immunol* **58**, 642-648, doi:10.1111/j.1365-3083.2003.01344.x (2003).
- 25 Pattemore, P. K. & Jennings, L. C. *Chapter 31 - Epidemiology of Respiratory Infections*. 435-452 (2008).
- 26 Takahashi, K., Oharaseki, T., Yokouchi, Y., Hiruta, N. & Naoe, S. Kawasaki disease as a systemic vasculitis in childhood. *Ann Vasc Dis* **3**, 173-181, doi:10.3400/avd.sasvp01003 (2010).
- 27 Mason, W. H., Jordan, S. C., Sakai, R., Takahashi, M. & Bernstein, B. Circulating immune complexes in Kawasaki syndrome. *Pediatr Infect Dis* **4**, 48-51, doi:10.1097/00006454-198501000-00012 (1985).
- 28 Richards, J. O. *et al.* Optimization of antibody binding to Fc $\gamma$ RIIIa enhances macrophage phagocytosis of tumor cells. *Mol Cancer Ther* **7**, 2517-2527, doi:10.1158/1535-7163.MCT-08-0201 (2008).
- 29 Khor, C. C. *et al.* Genome-wide association study identifies FCGR2A as a susceptibility locus for Kawasaki disease. *Nat Genet* **43**, 1241-1246, doi:10.1038/ng.981 (2011).
- 30 Nagelkerke, S. Q. *et al.* Inhibition of Fc $\gamma$ RIII-mediated phagocytosis by IVIg is independent of IgG-Fc sialylation and Fc $\gamma$ RIIIb in human macrophages. *Blood* **124**, 3709-3718, doi:10.1182/blood-2014-05-576835 (2014).
- 31 Abe, J. *et al.* Gene expression profiling of the effect of high-dose intravenous Ig in patients with Kawasaki disease. *J Immunol* **174**, 5837-5845, doi:10.4049/jimmunol.174.9.5837 (2005).
- 32 Shana Godfred-Cato, D. *et al.* COVID-19–Associated Multisystem Inflammatory Syndrome in Children — United States, March–July 2020. *MMWR Morb Mortal Wkly Rep* **69**, 1074-1080, doi:10.15585/mmwr.mm6932e2external icon (2020).
- 33 Ibarrondo, F. J. *et al.* Rapid Decay of Anti-SARS-CoV-2 Antibodies in Persons with Mild Covid-19. *N Engl J Med*, doi:10.1056/NEJMc2025179 (2020).
- 34 Gruber, C. N. *et al.* Mapping Systemic Inflammation and Antibody Responses in Multisystem Inflammatory Syndrome in Children (MIS-C). *Cell*, doi:10.1016/j.cell.2020.09.034 (2020).
- 35 Diorio, C. *et al.* Multisystem inflammatory syndrome in children and COVID-19 are distinct presentations of SARS-CoV-2. *J Clin Invest*, doi:10.1172/JCI140970 (2020).
- 36 Carter, M. J. *et al.* Peripheral immunophenotypes in children with multisystem inflammatory syndrome associated with SARS-CoV-2 infection. *Nat Med*, doi:10.1038/s41591-020-1054-6 (2020).
- 37 Lima, R. *et al.* Establishment of a Pediatric COVID-19 Biorepository: Unique Considerations and Opportunities for Studying the Impact of the COVID-19 Pandemic on Children. *Res Sq*, doi:10.21203/rs.3.rs-42030/v1 (2020).
- 38 Roy, V. *et al.* SARS-CoV-2-specific ELISA development. *J Immunol Methods* **484-485**, 112832, doi:10.1016/j.jim.2020.112832 (2020).
- 39 Fischinger, S. *et al.* A high-throughput, bead-based, antigen-specific assay to assess the ability of antibodies to induce complement activation. *J Immunol Methods* **473**, 112630, doi:10.1016/j.jim.2019.07.002 (2019).
- 40 Ackerman, M. E. *et al.* A robust, high-throughput assay to determine the phagocytic activity of clinical antibody samples. *J Immunol Methods* **366**, 8-19, doi:10.1016/j.jim.2010.12.016 (2011).
- 41 Karsten, C. B. *et al.* A versatile high-throughput assay to characterize antibody-mediated neutrophil phagocytosis. *J Immunol Methods* **471**, 46-56, doi:10.1016/j.jim.2019.05.006 (2019).

- 42 Mahan, A. E. *et al.* A method for high-throughput, sensitive analysis of IgG Fc and Fab glycosylation by capillary electrophoresis. *J Immunol Methods* **417**, 34-44, doi:10.1016/j.jim.2014.12.004 (2015).
- 43 McInnes, L., Healy, J. & Melville, J. UMAP: Uniform Manifold Approximation and Projection for Dimension Reduction. *arXiv preprint* (2018).
- 44 Wold, S., Esbensen, K. & Geladi, P. Principal component analysis. *Chemometrics and Intelligent Laboratory Systems* **2**, 37-52, doi:10.1016/0169-7439(87)80084-9 (1987).
- 45 Tibshirani, R. Regression shrinkage and selection via the lasso: a retrospective. *J. R. Statist. Soc. B* **73**, 273-282 (2011).

## Figure Legends

### Figure 1: Disease severity tracks with enhanced humoral immunity to COVID-19.

SARS-CoV-2 specific plasma antibody responses in mild (non-hospitalized) or severe (hospitalized) adult COVID-19 patients and children with mild COVID-19 patients were analyzed. A) SARS-CoV-2 Spike (S) protein specific IgM, IgG1 and IgA1 titers were analyzed by Luminex ( $n_{\text{mild}}=34$ ,  $n_{\text{severe}}=26$ ,  $n_{\text{children}}=25$ ). The dotted line represents the average plus 5 times the standard deviation of the negative plasma samples used to determine seropositivity (see Methods). B) IgG subclasses 1-4, isotypes IgM, IgA1 and IgA2, and antibody-mediated functions (complement deposition (ADCD), neutrophil phagocytosis (ADNP) and THP-1 monocyte phagocytosis (ADCP)) for SARS-CoV-2 RBD, S and N were analyzed in all seropositive individuals ( $n_{\text{mild}}=17$ ,  $n_{\text{severe}}=26$ ,  $n_{\text{children}}=15$ ). Each flower plot summarizes the data from the respective group and each petal represents the average of the Z-scored value for the indicated feature (Supplemental Figures 1-4). C) Univariate comparison of ADCD, ADNP and ADCP against SARS-CoV-2 S in seropositive individuals are shown. The dashed line in the violin plots indicate the median per group and solid lines indicate quartiles. A non-parametric Kruskal-Wallis test was used to test for statistically significant differences between multiple groups (\*: $p<0.05$ , \*\*: $p\leq 0.01$ , \*\*\*: $p<0.001$ , \*\*\*\*: $p\leq 0.0001$ ).

### Figure 2: SARS-CoV-2 specific IgA titers and augmented antibody functionality discriminate severe from mild disease.

Pair-wise comparisons were performed between seropositive mild diseased children and severely ill adults (A and D), mild and severe diseased adults (B and E) or mild diseased children and adults (C and F) ( $n_{\text{mild}}=17$ ,  $n_{\text{severe}}=26$ ,  $n_{\text{children}}=15$ ). A, B, C) Multivariate UMAP analyses show the variation in the multivariate humoral profiles across the groups. Proximity of points indicate homology in the overall dataset. D, E, F). In a second approach, a supervised multivariate comparison was performed across groups, where features were initially reduced using LASSO, to avoid overfitting, and then visualized by

PLS-DA (left panel). Cross-validation accuracy for D, E, F) was: 0.91, 0.97, 0.65, respectively. The LASSO selected features were also plotted and ranked in a VIP score plot (right panel, color of bars indicate in which group the feature was enriched). G) Network correlations depict the additional non-LASSO-selected Fc-profile features (small circles) that were correlated with the LASSO selected features (big circles) based on pair-wise comparisons between children and severely ill adults. The connections between points (features) indicate significant ( $p > 0.05$ ) Spearman correlations. Fill color of the circles indicate in which group the selected feature were enriched (grey = feature was not selected), the color of connecting lines indicate the strengths of the correlation coefficient.

**Figure 3. Unique functional and evolutionary profiles of SARS-CoV-2 IgA antibodies.** The matched-line graphs show the impact of IgG (A) and IgA (B) and IgG+IgA (C) depletion on ADNP activity across severely ill adults (dark blue), mildly ill adults (red), or children with mild disease (light blue). (D) The bar graphs show the level of degranulation of MPO, lactoferrin and MMP-9, and cytokine secretion of IL-1 $\beta$ , IL-6, and IL-8 in naïve/undepleted plasma compared to IgG or IgA depleted plasma. (E) The principal component analysis highlights the multivariate functional profiles observed in undepleted, IgG or IgA depleted plasma, highlighting the distinct inflammatory cascades associated with IgA depletion (light blue) that intermingled with IgG depleted plasma (medium blue), both of which were distinct from naïve undepleted plasma (black). (F) The line graphs show the longitudinal evolution of IgA1, IgA2, Fc $\alpha$ R binding, and ADNP over time in a group of severely (n=33) or moderately (n=28) ill individuals followed over the course of the first 2 weeks following symptom onset. Statistical significance in A-C was calculated by non-parametric Wilcoxon matched-pairs signed rank test and a parametric One-way ANOVA in D. A Mann-Whitney test was used to assess statistical difference between the groups at each interval. P-values were corrected for multiple hypothesis testing using the Benjamini-Hochberg procedure. (\*:  $p \leq 0.05$ , \*\*:  $p < 0.01$ , \*\*\*:  $p < 0.001$ , ns: not-significant).

**Figure 4: Distinct SARS-CoV-2 specific antibody responses in children with severe MIS-C.**

SARS-CoV-2 specific plasma antibody responses were analyzed in children with mild or severe MIS-C or convalescent adults. A) SARS-CoV-2 Spike (S) protein specific IgM, IgG1 and IgA1 titers were analyzed by Luminex ( $n_{\text{conv}}=18$ ,  $n_{\text{mild}}=6$ ,  $n_{\text{severe}}=11$ ). The dotted line represents the average plus 5 times the standard deviation of the negative plasma samples used to determine seropositivity (see Methods). B) IgG subclasses 1-4, isotypes IgM, IgA1 and IgA2, and antibody-mediated functions (ADCD, ADNP, and ADCP) for SARS-CoV-2 RBD, S and N in all seropositive individuals were analyzed ( $n_{\text{conv}}=18$ ,  $n_{\text{severe}}=9$ ). Each flower plot summarizes the data of the respective group and each petal represents the average of the Z-scored value for the indicated feature (Supplemental Figures 1-4). C) Univariate analysis of ADCD, ADNP, and ADCP against SARS-CoV-2 S are shown. Dashed lines in the violin plots indicate the median per group and solid lines indicate quartiles. A non-parametric Mann-Whitney test was used to test for statistically significant differences between the two groups (\*: $p<0.05$ , \*\*:: $p\leq 0.01$ , \*\*\*: $p<0.001$ , \*\*\*\*: $p\leq 0.0001$ ).

**Figure 5: Dysregulated and pro-inflammatory antibody-profiles in children with severe MIS-C.**

Pairwise comparisons by UMAP and LASSO/PLS-DA analyses are shown across mild and severe MIS-C (A), severe MIS-C and convalescent (B) or severe MIS-C and acutely infected children (C) ( $n_{\text{mild\_MIS-C}}=6$ ,  $n_{\text{severe MIS-C}}=9$ ,  $n_{\text{SARS+ children}}=15$ ,  $n_{\text{convalescent}}=18$ ). The size of each dot represents the log10 scaled value of IgG1 titer to SARS2 RBD. The cross-validation accuracy in B) and C) were: 0.89, 0.88, respectively. D) The correlation network of LASSO selected (big circles) or unselected (small circles) features are shown across children and severely ill adults. Connection between points (features) indicate significant relationships ( $p>0.05$ ) defined by a Spearman correlation after Benjamini-Hochberg correction. Fill



color of the circles indicate in which group the selected feature was enriched (grey = feature was not selected), the color of the connecting lines indicate the correlation coefficient. E) The chord diagrams show the relationships of Luminex defined IgG1 titers across SARS-CoV-2 antigens (upper panel, yellow =RBD, red =S, and blue =N) and other pathogens and auto-antigens (lower panel, yellow = common CoVs RBD, red = other respiratory viruses, blue = KD associated pathogens, green = MIS-C associated auto-antigens) assessed by Spearman correlation. The connecting lines between colored boxes (antigen-specific IgG1 titer) and grey boxes (FcγRs) indicate a significant ( $p<0.05$ ) correlation between antigen-specific IgG1 titers and binding to the indicated FcγR for the respective antigen. A color-gradient was used to indicate the correlation coefficient (from  $r=-1$  (dark blue) over  $r=0$  (white) to  $r=1$  (dark red)) for the individual correlations.

**Supplemental Figure 1:** Analysis of SARS-CoV-2 RBD specific IgM (A), IgG1 (B), IgG2 (C), IgG3 (D), IgG4 (E), IgA1 (F), IgA2 (G), FcγR2a (H), FcγR2b (I), FcγR3a (J), FcγR3b (K), FcαR (L) and FcRn (M) ( $n_{\text{mild}}=34$ ,  $n_{\text{severe}}=26$ ,  $n_{\text{SARS+ children}}=25$ ,  $n_{\text{mild\_MIS-C}}=6$ ,  $n_{\text{severe MIS-C}}=11$ ,  $n_{\text{convalescent}}=18$ ). The dotted line represents the average plus 5 times the standard deviation of the negative plasma samples used to determine seropositivity (see Methods). A non-parametric Kruskal-Wallis test was used to test for statistically significant differences between multiple groups (\*: $p<0.05$ , \*\*: $p<0.01$ , \*\*\*: $p<0.001$ , \*\*\*\*: $p<0.0001$ ). These data were also compiled in flower plots in Figure 1 and 4, for multivariate visualization.

**Supplemental Figure 2:** Analysis of SARS-CoV-2 S specific IgM (A), IgG1 (B), IgG2 (C), IgG3 (D), IgG4 (E), IgA1 (F), IgA2 (G), FcγR2a (H), FcγR2b (I), FcγR3a (J), FcγR3b (K), FcαR (L) and FcRn (M) ( $n_{\text{mild}}=34$ ,  $n_{\text{severe}}=26$ ,  $n_{\text{SARS+ children}}=25$ ,  $n_{\text{mild\_MIS-C}}=6$ ,  $n_{\text{severe MIS-C}}=11$ ,  $n_{\text{convalescent}}=18$ ). The dotted line represents the average plus 5 times the standard deviation of the negative plasma samples used to determine seropositivity (see Methods). A non-parametric Kruskal-Wallis test was used to test for statistically significant differences between multiple groups (\*: $p<0.05$ , \*\*: $p<0.01$ , \*\*\*: $p<0.001$ , \*\*\*\*: $p<0.0001$ ). Data from graphs in A, B and F are also included in Figures 1 or 4 as flower plots.

**Supplemental Figure 3:** Analysis of SARS-CoV-2 N specific IgM (A), IgG1 (B), IgG2 (C), IgG3 (D), IgG4 (E), IgA1 (F), IgA2 (G), FcγR2a (H), FcγR2b (I), FcγR3a (J), FcγR3b (K), FcαR (L) and FcRn (M) ( $n_{\text{mild}}=34$ ,  $n_{\text{severe}}=26$ ,  $n_{\text{SARS+ children}}=25$ ,  $n_{\text{mild\_MIS-C}}=6$ ,  $n_{\text{severe MIS-C}}=11$ ,  $n_{\text{convalescent}}=18$ ). The dotted line represents the average plus 5 times the standard deviation of the negative plasma samples used to determine seropositivity (see Methods). A non-parametric Kruskal-Wallis test was used to test for statistically significant differences between multiple groups (\*: $p<0.05$ , \*\*:  $p\leq 0.01$ , \*\*\*: $p<0.001$ , \*\*\*\*: $p\leq 0.0001$ ). These data have also been included as flower plots in Figure 1 and 4.

**Supplemental Figure 4:** SARS-CoV-2 RBD (A), S (B) and N (C) specific antibody-dependent complement deposition (ADCD). SARS-CoV-2 RBD (D), S (E) and N (F) specific antibody-dependent neutrophil phagocytosis (ADNP) and SARS-CoV-2 RBD (G), S (H) and N (I) specific antibody-dependent monocyte phagocytosis (ADCP) were assessed across  $n_{\text{mild adults}}=17$ ,  $n_{\text{severe adults}}=26$ ,  $n_{\text{children}}=15$ ,  $n_{\text{conv}}=18$ ,  $n_{\text{severe MIS-C}}=9$ . A non-parametric Kruskal-Wallis test was used to test for statistically significant differences between multiple groups and Mann-Whitney test was used to test for statistically significant differences between the two groups (\*: $p<0.05$ , \*\*:  $p\leq 0.01$ , \*\*\*: $p<0.001$ , \*\*\*\*: $p\leq 0.0001$ ). Graphs in B, E and H have also been included in Figures 1 or 4, as flower plots for multivariate visualization.

**Supplemental Figure 5: Time dependency of SARS-CoV-2 specific antibody responses in acute disease.** IgM (A), IgG1 (B), IgA1 (C) and ADNP (D) responses against SARS-CoV-2 S are shown for mildly ill children, adults with mild disease, or severely ill adults from the day of symptom onset.

**Supplemental Figure 6:** A) A three-way UMAP analysis shows the comparison of the multivariate SARS-CoV-2-specific humoral response across severely ill adults, mildly ill adults, and children. B) The LASSO/PLS-DA analysis shows the comparison of SARS-CoV-2 specific antibody profiles across age-groups, split along a median age split (55 years). The model was not significant (cross-validation

accuracy: 0.5895). C) Instead, the same LASSO/PLS-DA as in B) was colored by disease severity (mild or severe), age is indicated by symbol, demonstrating better separation.

**Supplemental Figure 7:** The Correlation network shows the analysis of LASSO selected (big circles) or non-selected (small circles) features that were selectively enriched across mild and severely ill adults. Connections between points (features) indicate significant ( $p > 0.05$ ) Spearman correlations. Fill colors of the circles indicate the specific group in which the selected feature was enriched (grey = feature was not selected), the color of connecting lines indicates the correlation coefficient (compare Figure 2).

**Supplemental Figure 8:** Plasma samples from severely ill adult COVID19 patients were pooled and IgA and/or IgG were subsequently depleted. (A) The line graph shows the confirmed isotype specific depletion of S-specific antibodies by (S)-specific IgG, IgA and IgM ELISA. (B) The graph indicates the primary neutrophil derived cytokine secretion profiles across three healthy donors following a 4 hour stimulation with SARS-CoV-2 S specific immune complexes. The release of IL-18, GM-CSF and TNF $\alpha$  were determined by multiplex cytokine luminex.

**Supplemental Figure 9:** (A) Pairwise comparisons by UMAP and LASSO/PLS-DA analyses are shown for children with severe MIS-C and severe acutely infected adults ( $n_{\text{severe MIS-C}}=9$ ,  $n_{\text{severe-adults}}=26$ ) with a cross-validation accuracy of 0.99. B) The correlation network of LASSO selected (big circles) or unselected (small circles) features are shown across children and severely ill adults. Connection between points (features) indicate significant relationships ( $p > 0.05$ ) defined by a Spearman correlation after Benjamini-Hochberg correction. Fill color of the circles indicate in which group the selected feature were enriched (grey = feature was not selected), the color of connecting lines indicate the correlation coefficient.

**Supplemental Figure 10:** (A) The graph shows the time course of the S-specific humoral IgM, IgG1 and IgA1 titers and (B) ADCD, ADNP and ADCP functions in five severe MIS-C patients (compare Patients # with Supplemental Table 2).

**Supplemental Figure 11:** The heatmap shows IgG1 (A) and IgM (B) antibody levels against different SARS-CoV-2, common CoVs, other respiratory viruses, KD associated pathogens and MIS-C associated auto-antigens. Values were Z-scored and the average value for each group and antigen was plotted. Some data in this figure has been published elsewhere<sup>3</sup>. (C) The chord diagrams show the relationships of Luminex defined IgG1 titers across SARS-CoV-2 antigens (upper panel, yellow =RBD, red =S, and blue =N) and other pathogens and auto-antigens (lower panel, yellow = common CoVs RBD, red = other respiratory viruses, blue = KD associated pathogens, green = MIS-C associated auto-antigens) assessed by Spearman correlation. The connecting lines between colored boxes (antigen-specific IgG1 titer) and grey boxes (FcγRs) indicate a significant ( $p<0.05$ ) correlation between antigen-specific IgG1 titers and binding to the indicated FcγR for the respective antigen. A color-gradient was used to indicate the correlation coefficient (from  $r=-1$  (dark blue) over  $r=0$  (white) to  $r=1$  (dark red)) for the individual correlations.

**Supplemental Figure 12:** Total bulk IgM (A) and IgG (B) ELISA results are shown across plasma from SARS-CoV-2 infected (acute) or uninfected children, as well as children who developed mild or severe MIS-C. Additionally, the IgG-Fc glycosylation was analyzed by capillary electrophoresis. The frequency of IgG-Fc with agalactosylated (G0) (C), galactosylated but not sialylated (D), sialylated (E), fucosylated (F) or bisected (G) N-glycans are shown, respectively.

**Supplemental Figure 13:** The correlation of Luminex IgG1 and ELISA IgG titers against SARS-CoV-2 RBD (Spearman  $r^2= 0.53$ ,  $p<0.001$ ).

**Supplemental Figure 14:** The diagram shows the gating strategy for ADCP (A), HL-60 ADNP (B) and ADNP with primary human neutrophils (C).

**Supplemental Table 1: Study population demographic and clinical characteristics**

	<b>Adult mild COVID (n=34)</b>	<b>Adult severe COVID (n=26)</b>	<b>Adult convalescent (n=18)</b>	<b>pediatric mild COVID (n=25)</b>	<b>pediatric mild MIS-C (n=6)</b>	<b>pediatric severe MIS-C (n=11)</b>
Age, years, median (max, min)	34 (22, 76)	56 (32, 79)	33 (27, 58)	15 (0, 21)	1.8 (0.2, 9.7)	8.3 (1.5, 21.9)
Sex, male, n (%)	15 (44.1)	12 (46.2)	8 (44.4)	15 (60.0)	5 (83)	9 (82)
SARS-CoV-2 serostatus <sup>1</sup> , n positive (%)	17 (50.0)	26 (100)	18 (100)	13 (52.0)	0 (0)	9 (82)
Days since symptom onset, median (max,min)						
Overall	7 (0, 52)	16 (10, 37)	27 (11, 38)	3 (0, 21)	4.5 (2, 23)	5 (3, 21)
Seropositive	12.5 (2, 41)	16 (10, 37)	27 (11, 38)	7 (0, 21)	-	4.5 (3, 16) <sup>2</sup>
Clinical course, n (%)						
hospitalization	0	26 (100)	0	7 (28.0)	6 (100)	11 (100)
ICU treatment	0	15 (57.7)	0	1 (4)		

<sup>1</sup>Sero-status was defined by Luminex assay

<sup>2</sup> days of MIS-C symptoms

**Supplemental Table 2: Demographic, clinical characteristics and diagnostic criteria per CDC case definition of MIS-C patients (CDC: Center for Disease Control)**

					<b><i>CDC criteria for MIS-C</i></b>							<b><i>Disease progression</i></b>		
					<b>All of the following</b>				<b>One of the following</b>					
#	MIS-C severity	Age (years)	Sex	Race/ ethnicity	Symptoms	Laboratory evidence of inflammation	Multisystem organ involvement	No alternative plausible diagnosis	SARS-CoV-2 RT-PCR	SARS-CoV-2 antibodies	COVID-19 exposure	Hospital level of care	Cardiac involvement	Final Outcome
1	mild	0.1	F	unknown	fever, cough, vomiting, diarrhea	(+)	(+)	(+)	(+)	(+)	(+)	ward	none	discharged
2	mild	0.2	M	latino/ hispanic	fever, dyspnea	(+)	(+)	(+)	(+)		(+)	ward	none	discharged
3	mild	1.1	M	white	fever, cough	(+)	(+)	(+)			(+)	ward	none	discharged
4	mild	2.5	M	white	fever	(+)	(+)	(+)	(+)		(+)	ward	none	discharged
5	mild	2.9	M	white	fever, rash, vomiting, headache	(+)	(+)	(+)		(+)		ward	none	discharged
6	mild	9	M	white	fever, vomiting, diarrhea, myalgia, anosmia	(+)	(+)	(+)		(+)		ward	none	discharged
7	severe	1	M	african american	fever, chills	(+)	(+)	(+)		(+)		ward	coronary dilation	discharged
8	severe	2	F	asian	fever, fatigue	(+)	(+)	(+)	(+)	(+)	(+)	ward	mild pericardial effusion	discharged

9	severe	2.5	M	white	fever, rash, cough, sore throat	(+)	(+)	(+)			(+)	PICU	coronary dilation	discharged
10	severe	3.5	M	latino/hispanic	fever, rash	(+)	(+)	(+)		(+)	(+)	PICU	coronary dilation	discharged
11	severe	7	F	unknown	fever, vomiting, diarrhea	(+)	(+)	(+)	(+)	(+)	(+)	PICU	decreased ventricular function	discharged
12	severe	8.3	M	african american	fever, myalgia	(+)	(+)	(+)		(+)		PICU	ventricular failure: ecmo	discharged
13	severe	10	M	latino/hispanic	fever, rash	(+)	(+)	(+)	(+)	(+)	(+)	PICU	ventricular dilation and dysfunction	discharged
14	severe	12	M	latino/hispanic	fever, rash, dyspnea	(+)	(+)	(+)		(+)	(+)	PICU	coronary dilation, myocarditis	discharged
15	severe	13.5	M	white	fever, chills, headache	(+)	(+)	(+)	(+)	(+)		PICU	myocarditis	discharged
16	severe	19	M	white	fever, chest pain	(+)	(+)	(+)			(+)	PICU	ventricular failure: ecmo	discharged
17	severe	21.9	M	african american - latino/hispanic	fever, anorexia, vomiting, diarrhea	(+)	(+)	(+)		(+)		PICU	ventricular dilation and dysfunction	discharged



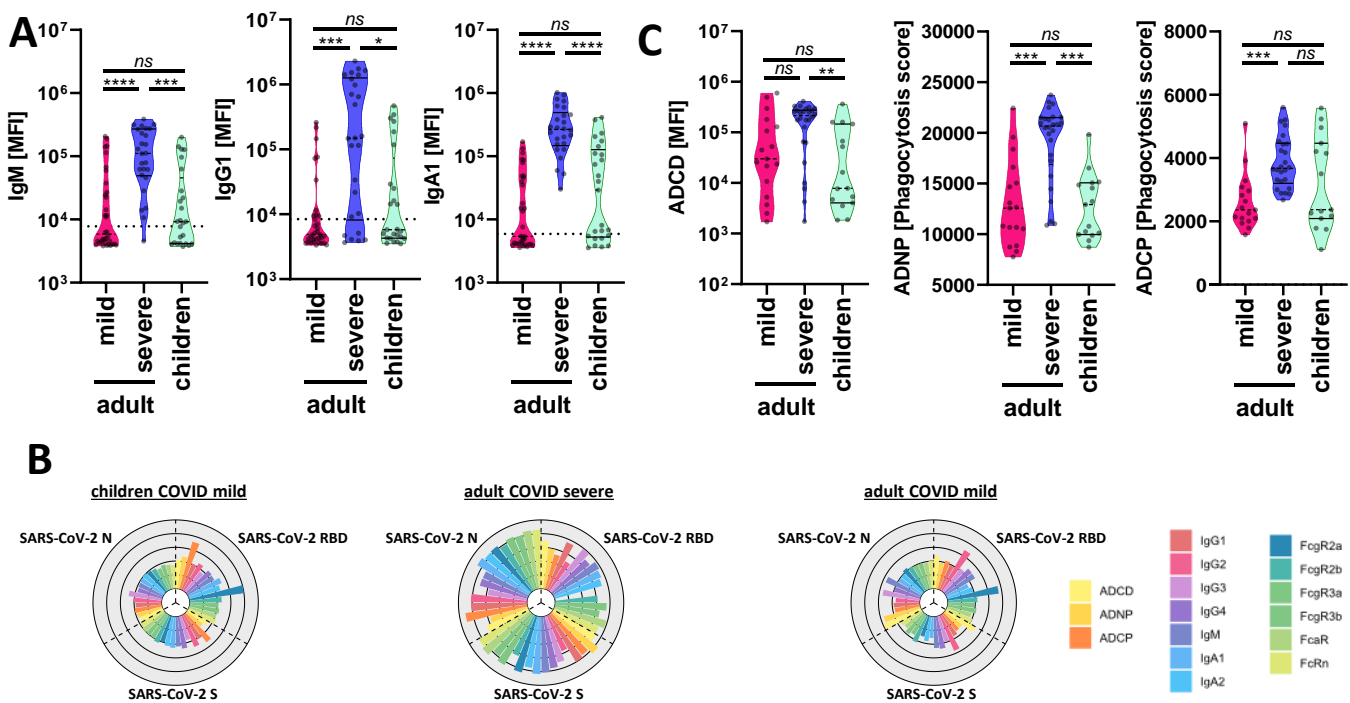


Figure 1

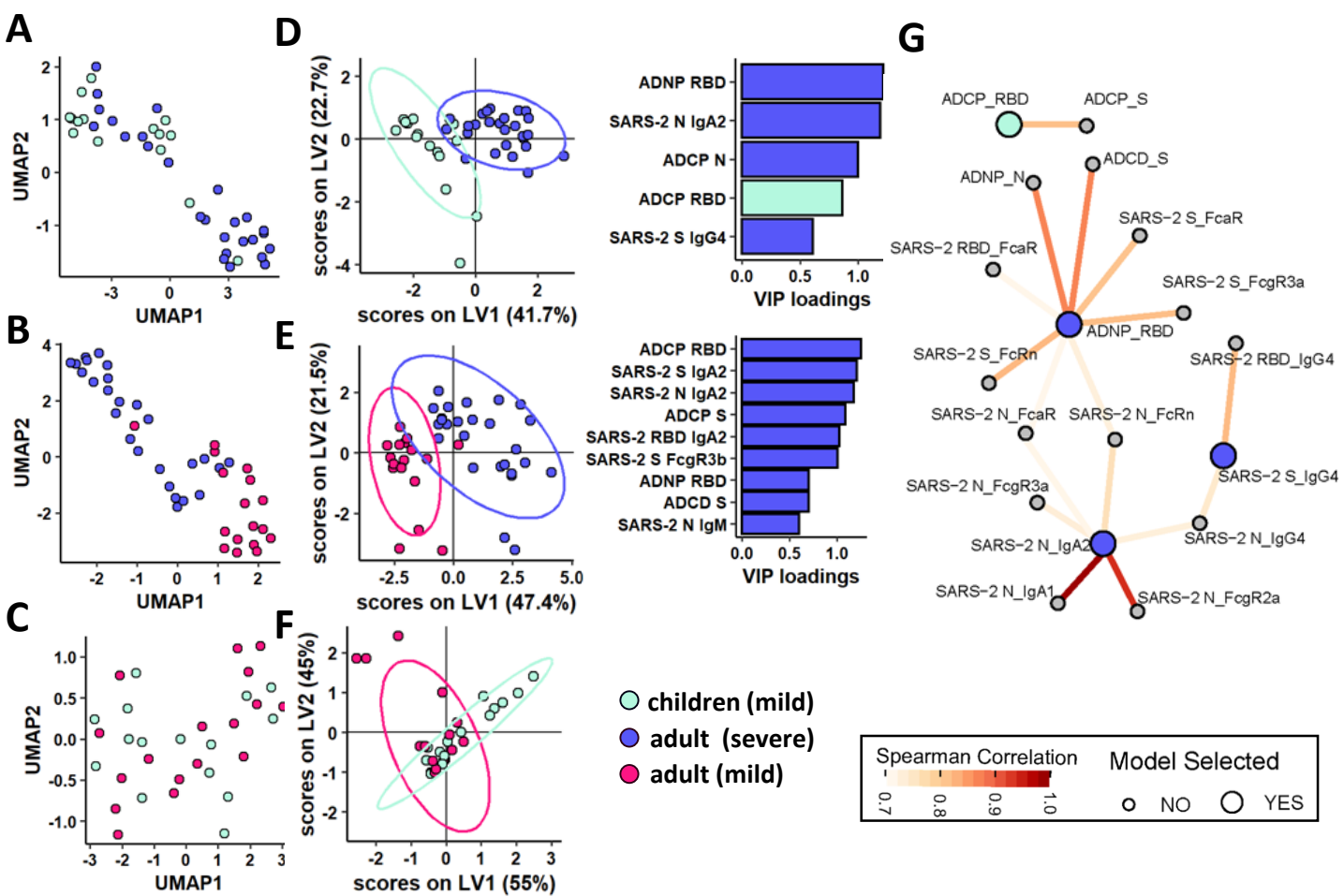


Figure 2

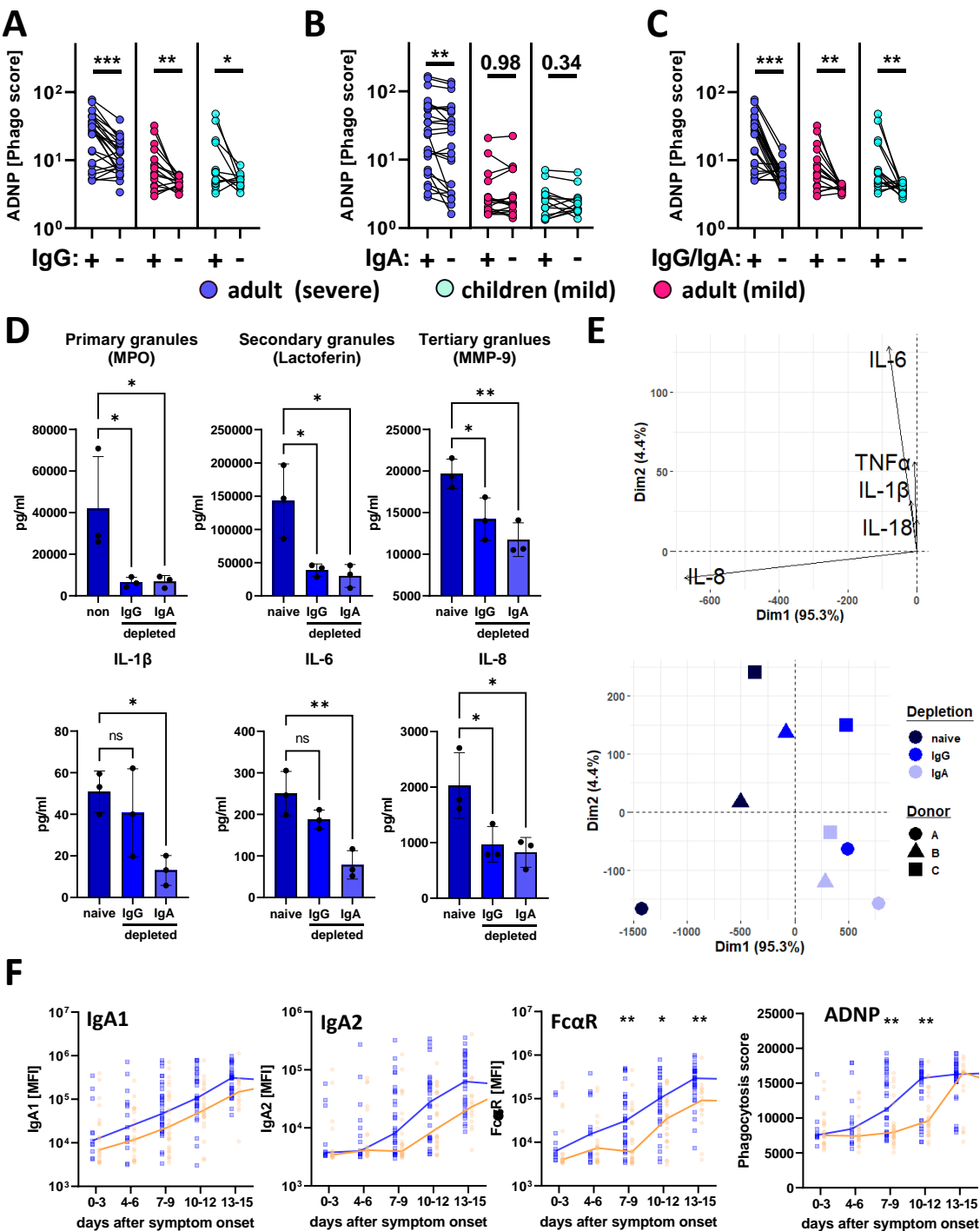


Figure 3

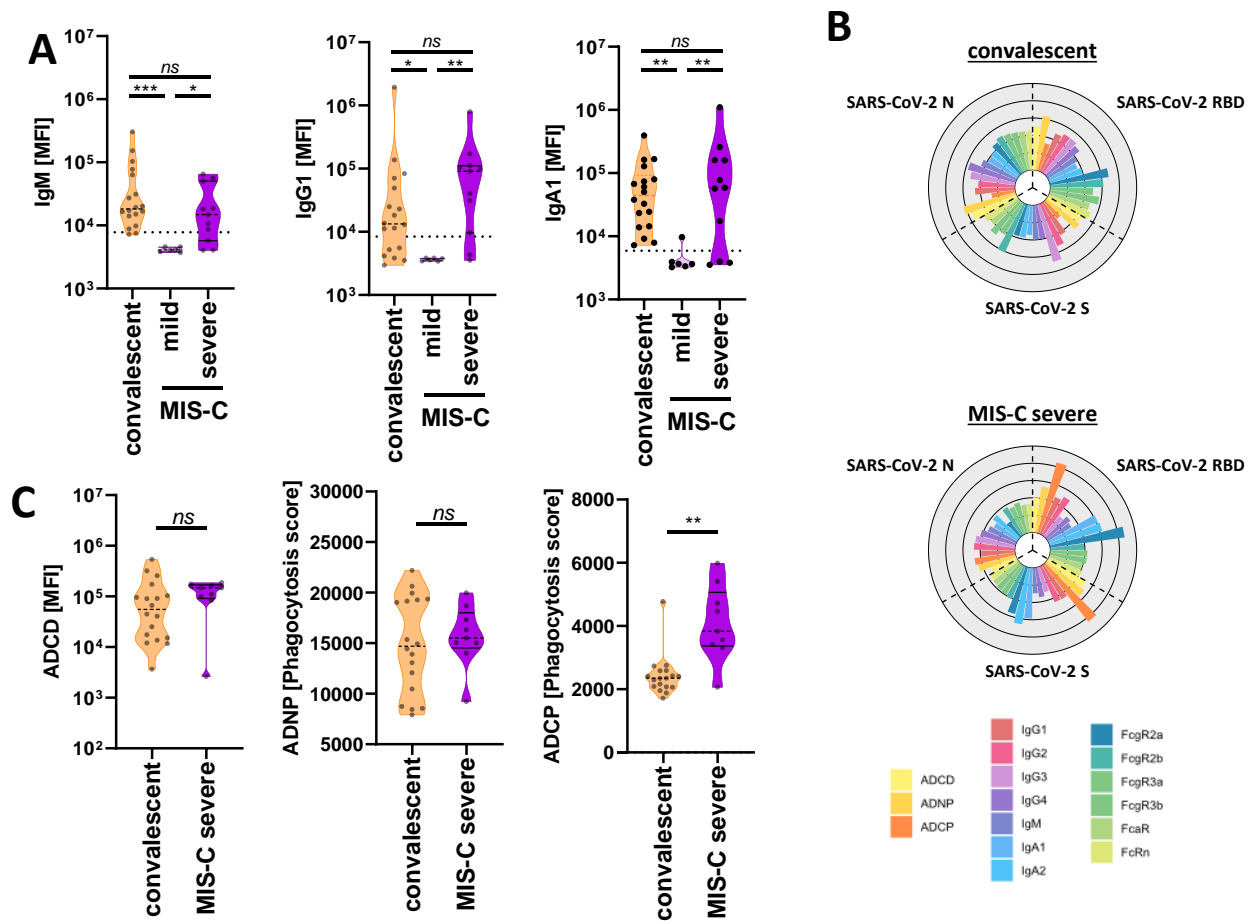


Figure 4

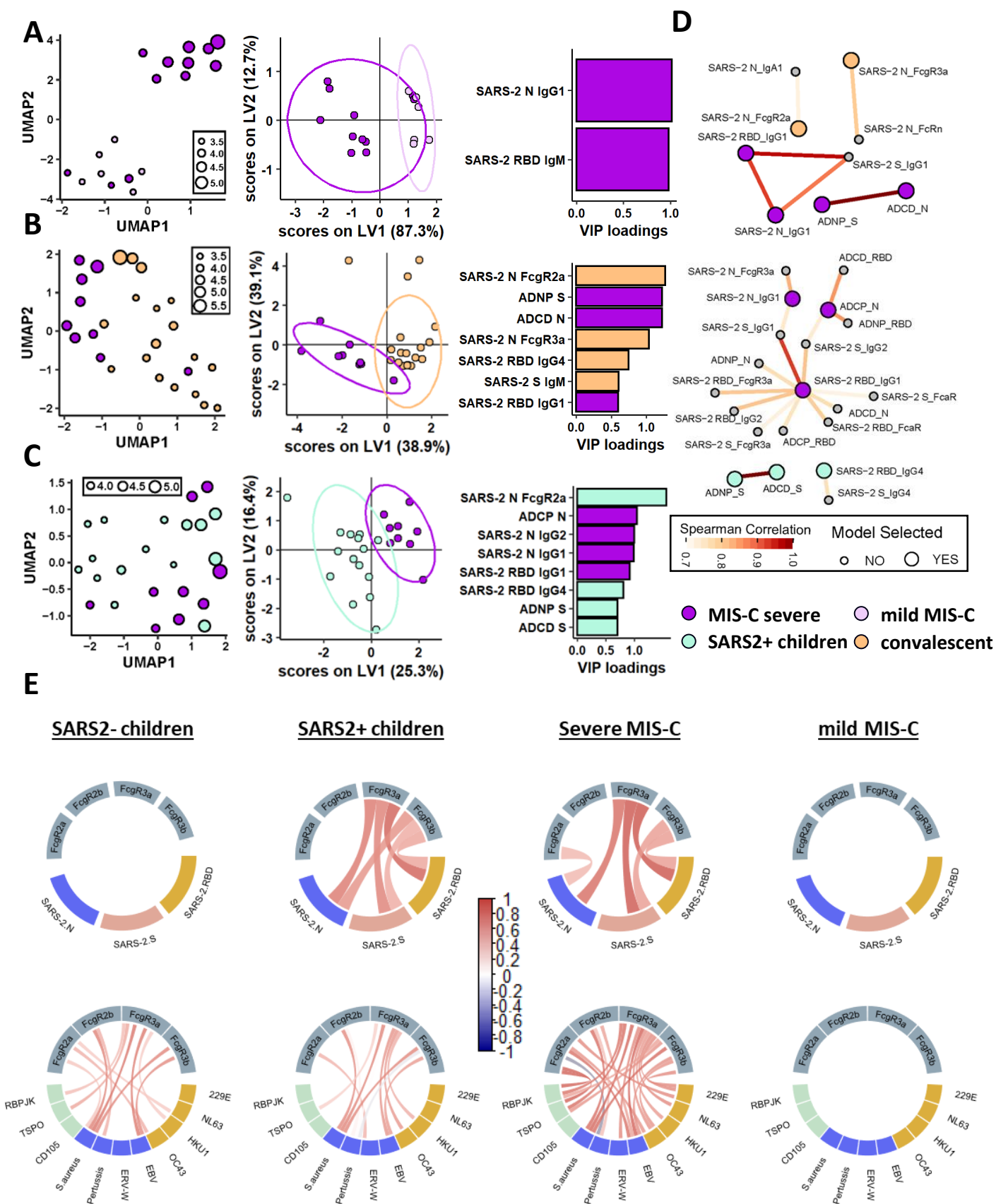
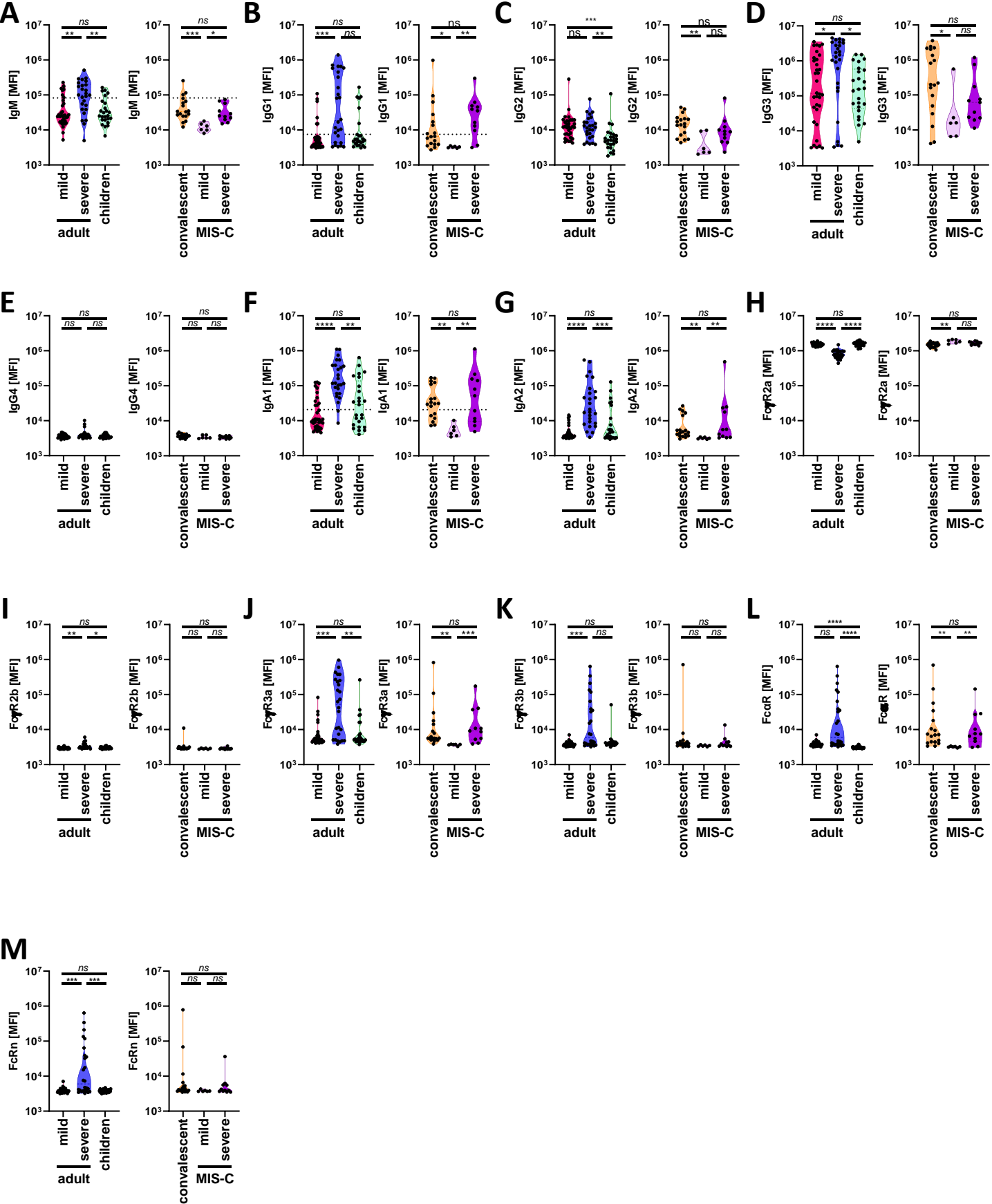
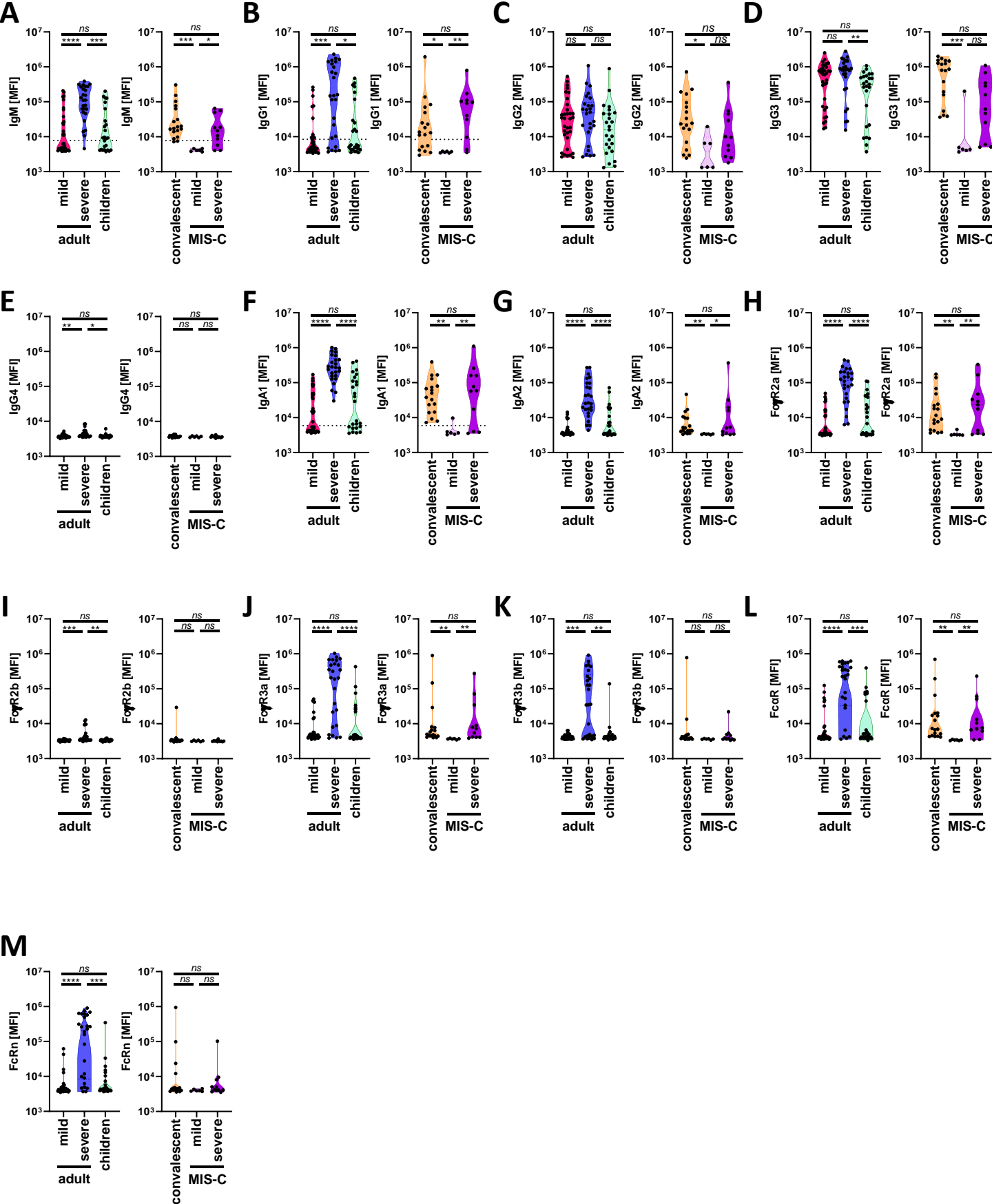


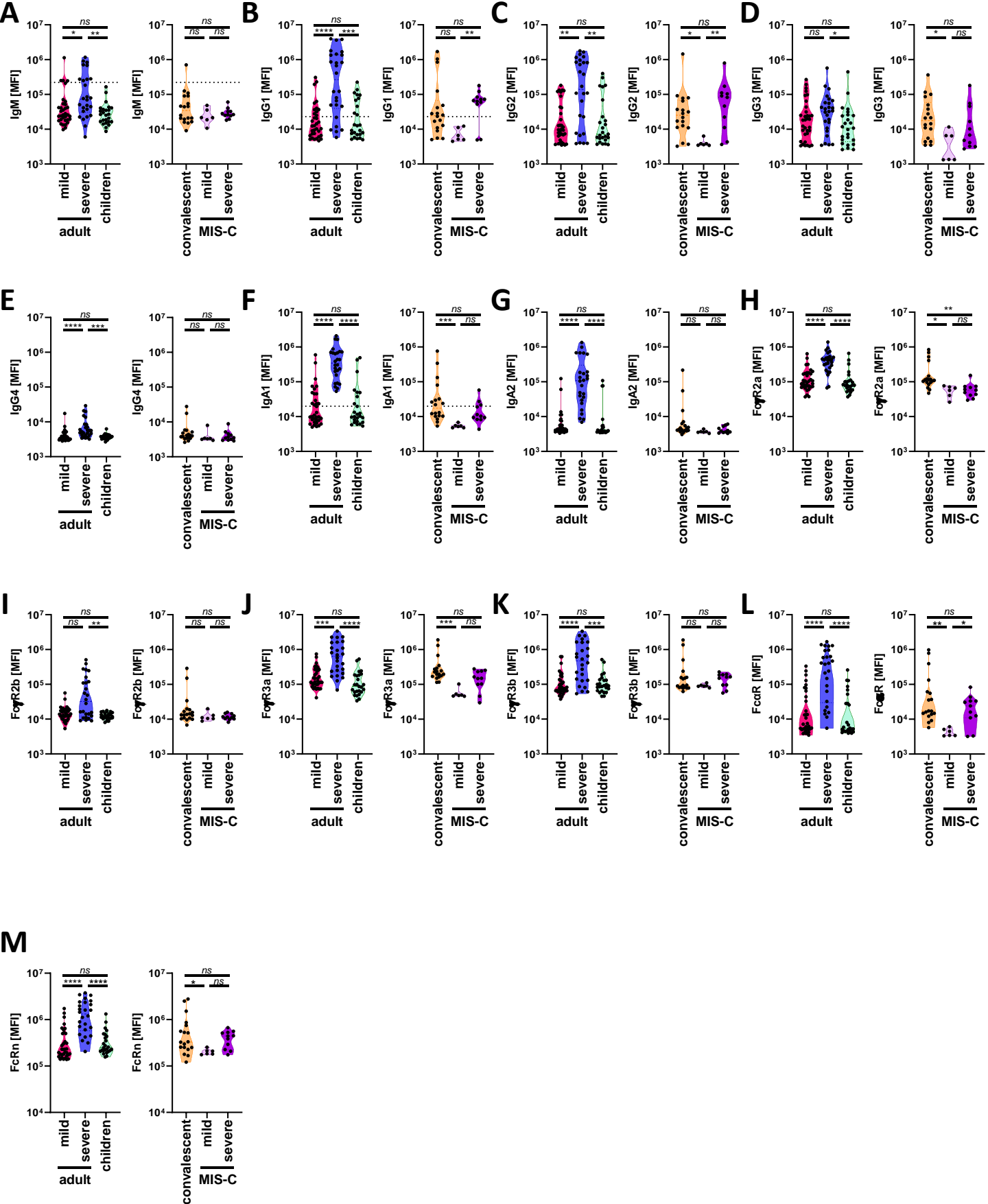
Figure 5



Supplemental Figure 1

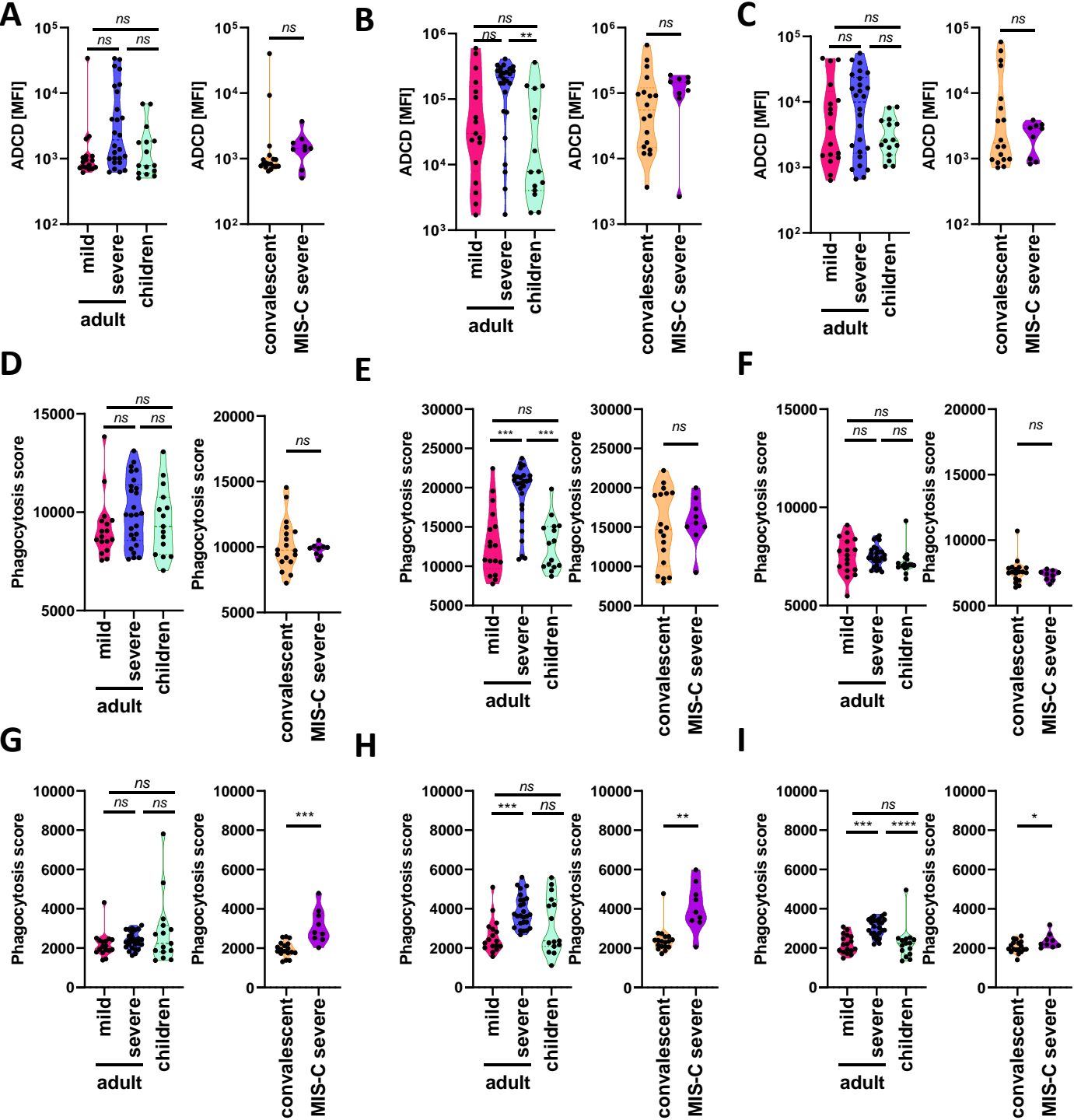


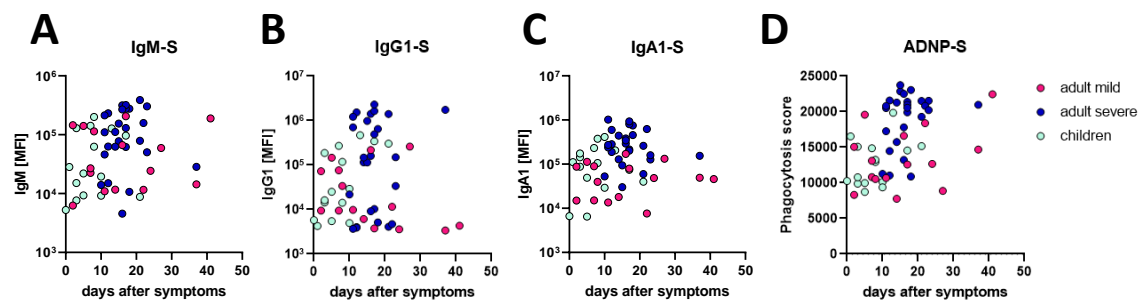
Supplemental Figure 2

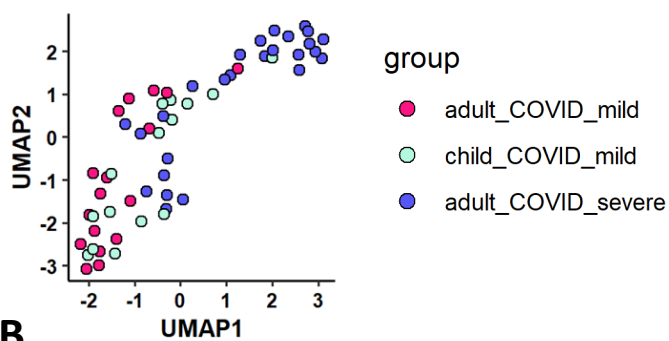
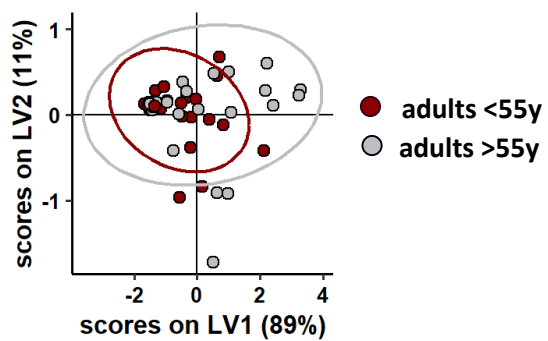
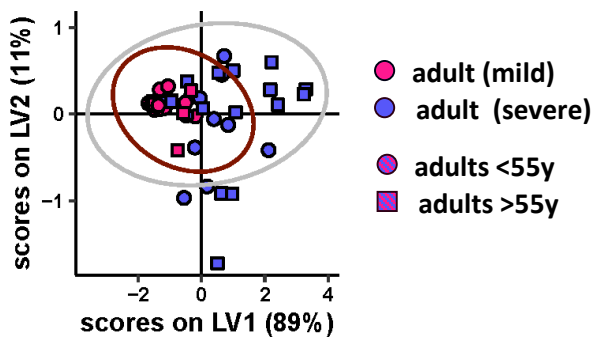


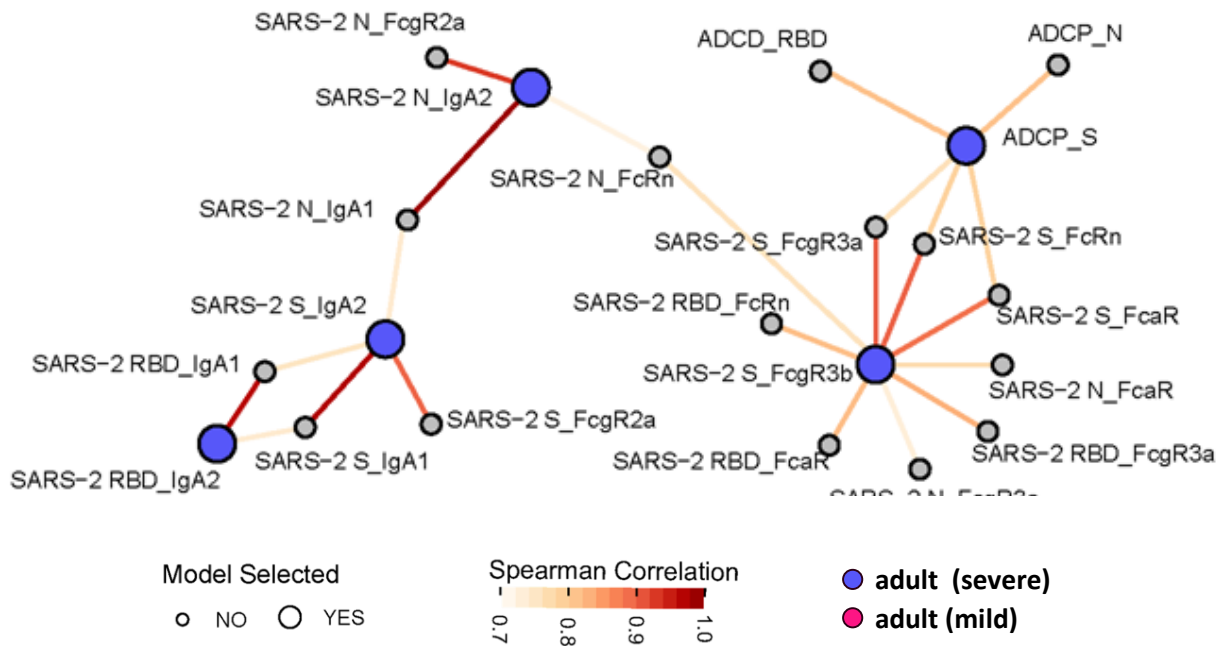
Supplemental Figure 3



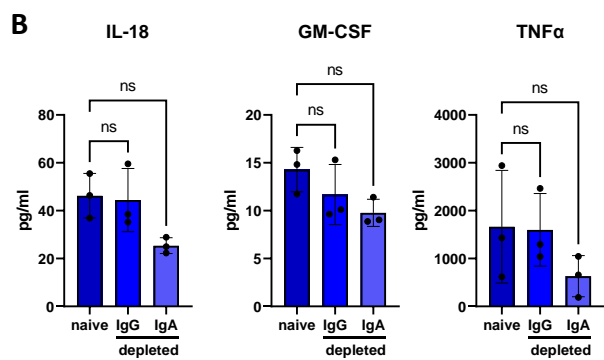
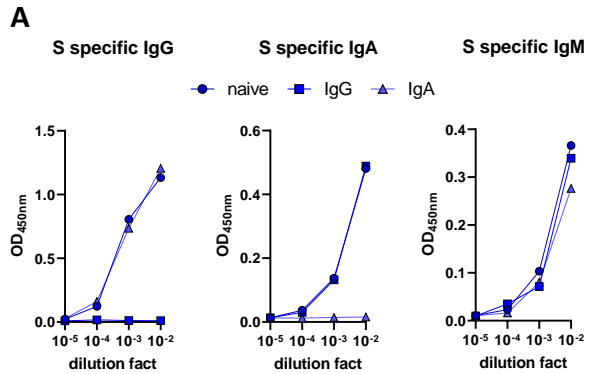


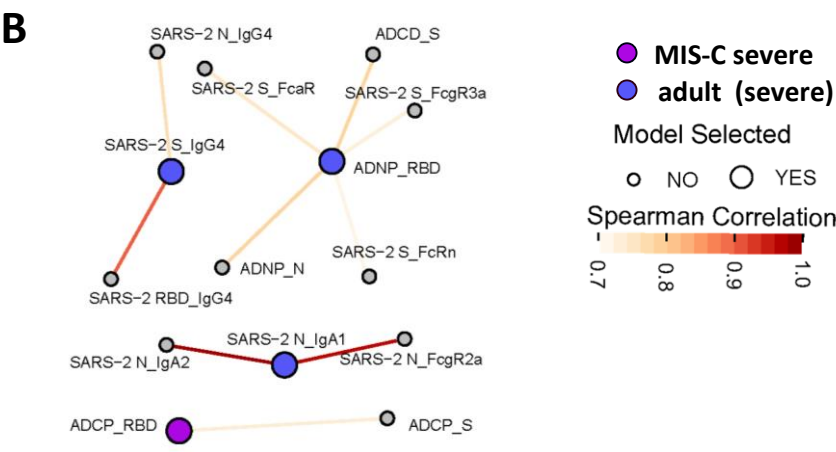
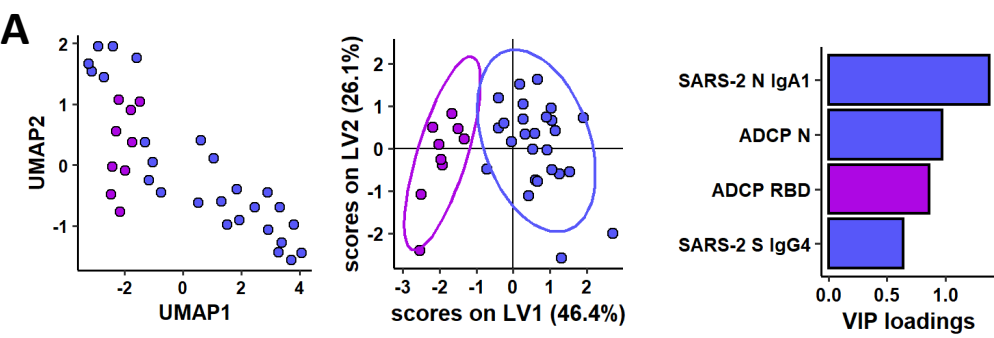


**A****B****C**

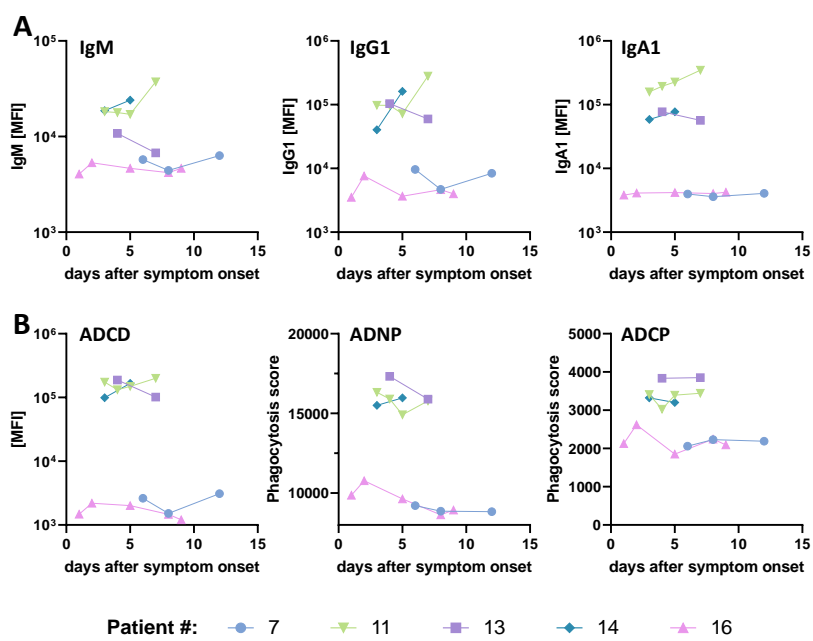


Supplemental Figure 7

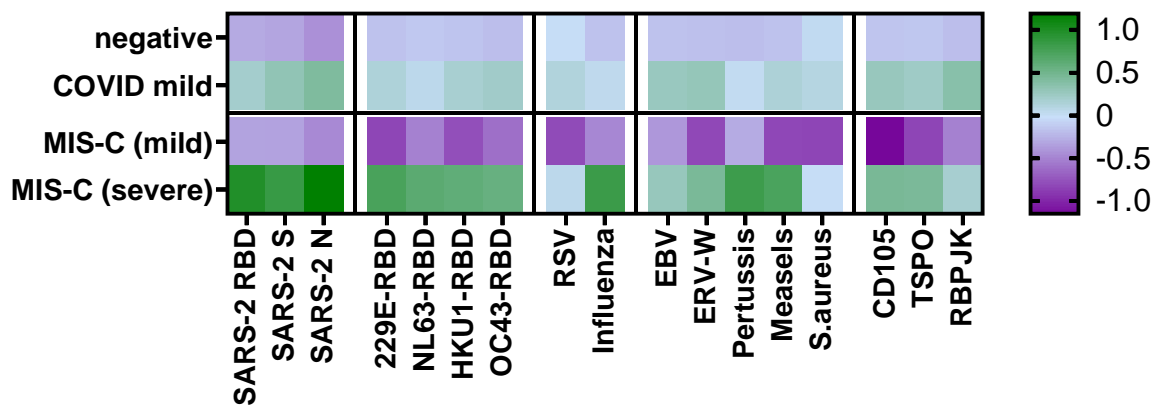




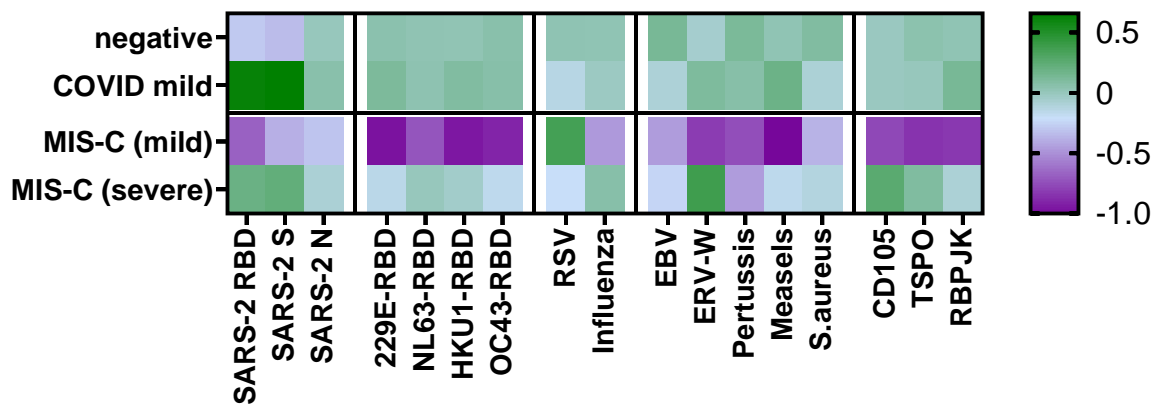
Supplemental Figure 9



A



B

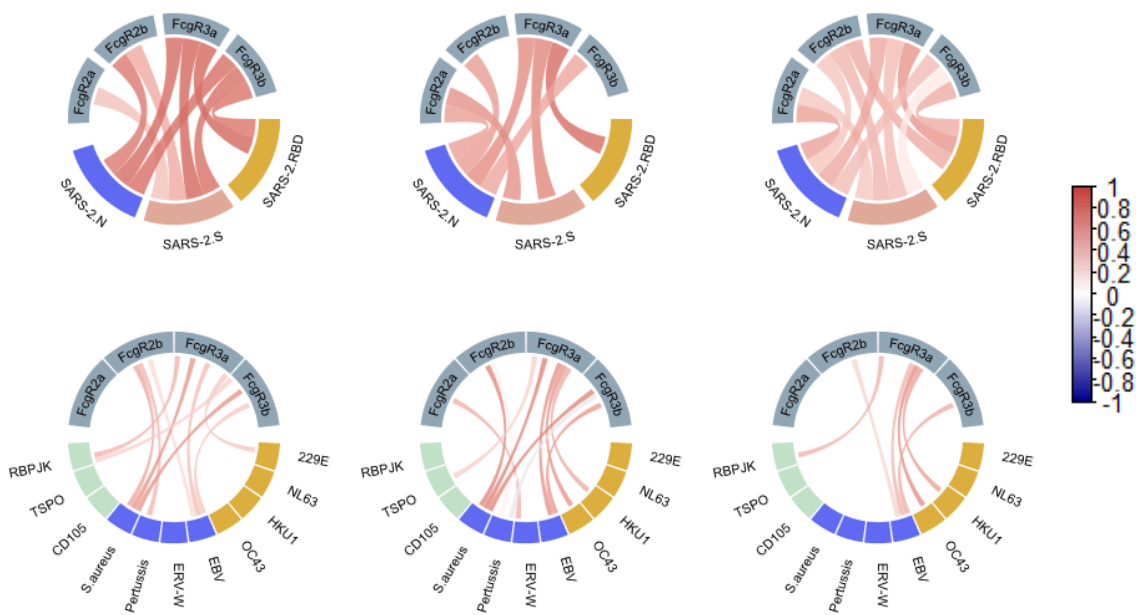


C

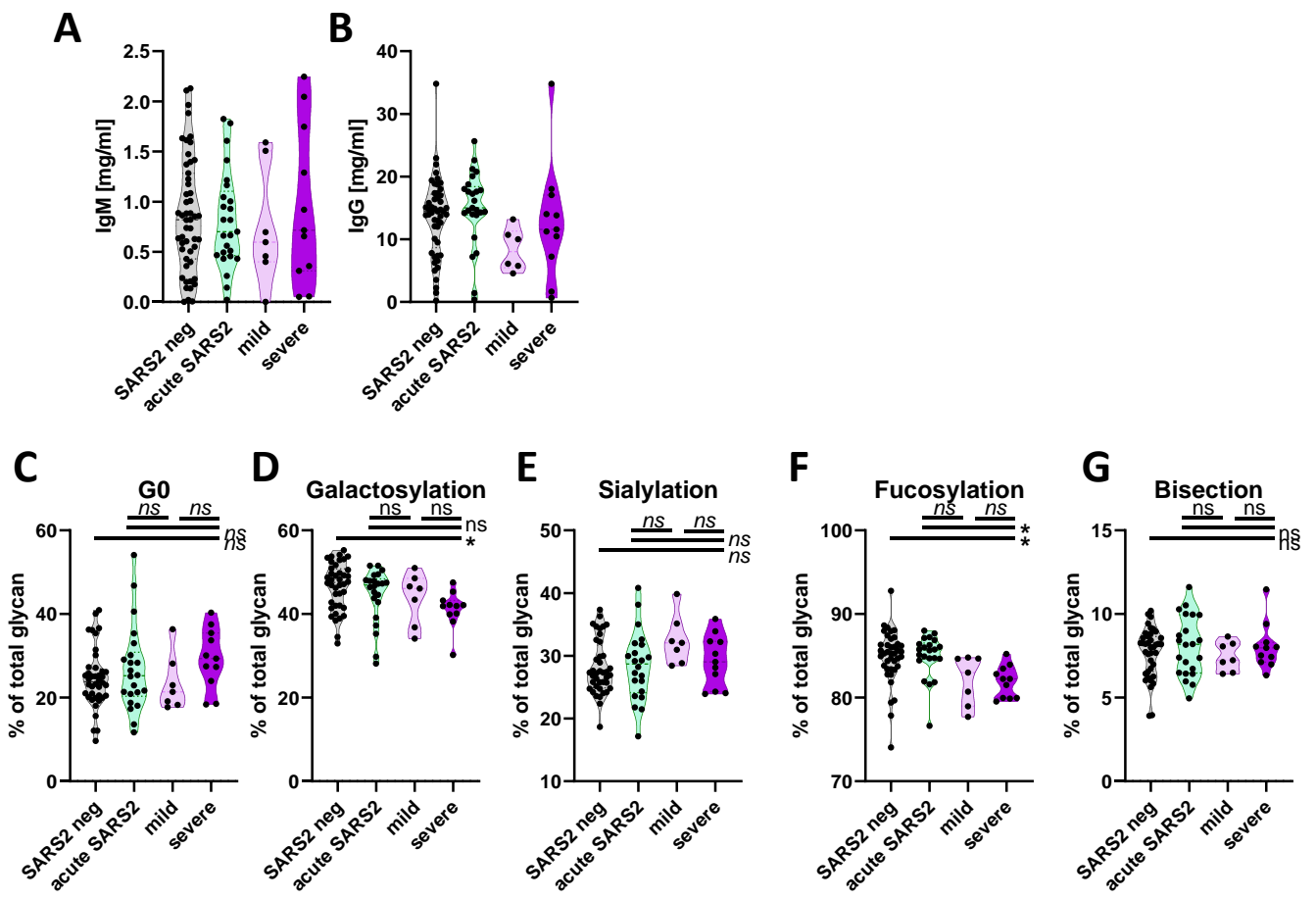
adult (severe)

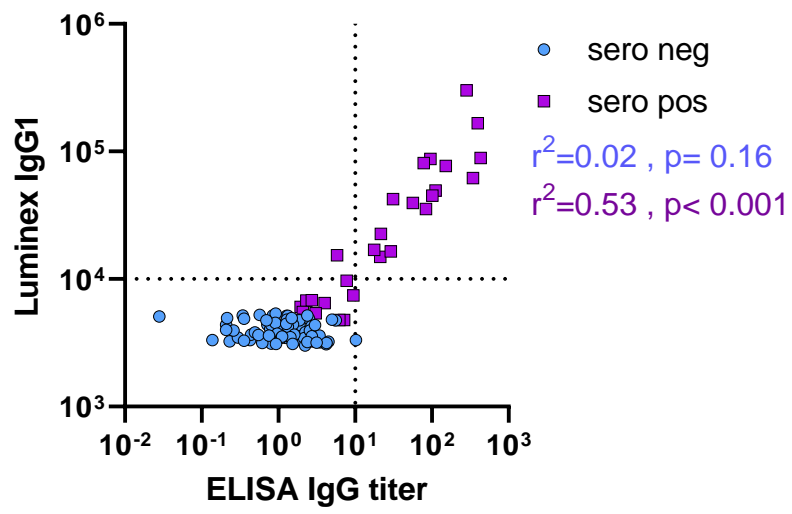
adult (mild)

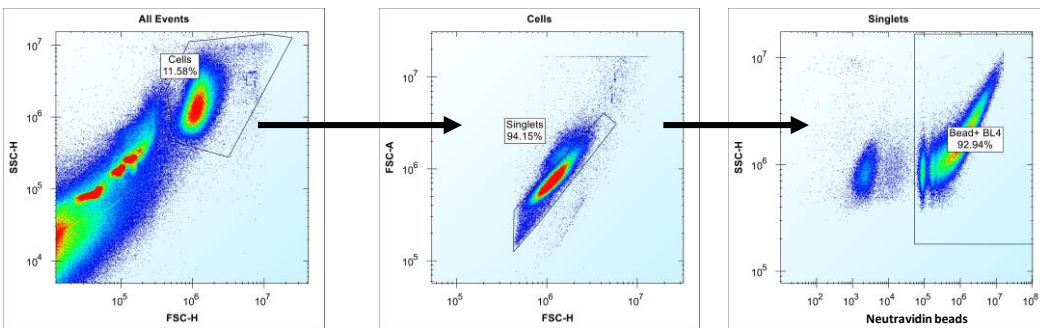
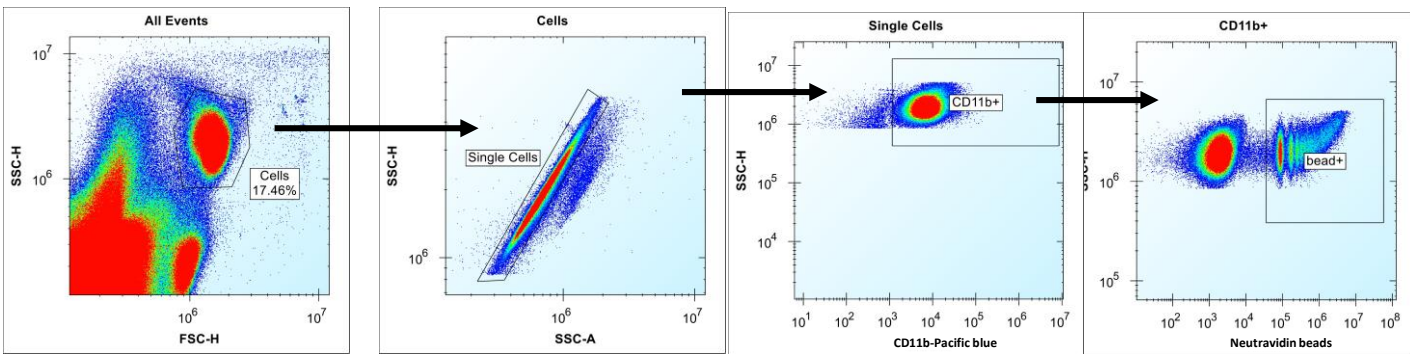
adult (convalescent)









**A****B****C**